photonics

MDPI

Article

Design and Performance Analysis of a Highly Sensitive Internal-Sensing PCF Biosensor for Early Malaria Detection

Noonepalle HariPriya [1,2], Mohammad Javad Maleki [3], Mohammad Soroosh [3,*], Haraprasad Mondal [4] and Sandip Swarnakar [1,*]

[1] Department of Electronics and Communication Engineering, Koneru Lakshmaiah Education Foundation, Vaddeswaram 522302, Andhra Pradesh, India; 2302041005@kluniversity.in
[2] Department of Electronics and Communication Engineering, Vallurupalli Nageswara Rao Vignana Jyothi Institute of Engineering &Technology, Bachupally, Hyderabad 500118, Telangana, India
[3] Department of Electrical Engineering, Shahid Chamran University of Ahvaz, Ahvaz 61357-85311, Iran; mj.maleki@scu.ac.ir
[4] Department of Electronics and Communication Engineering, Dibrugarh University, Dibrugarh 786004, Assam, India; mondal.haraprasad@dibru.ac.in
* Correspondence: m.soroosh@scu.ac.ir (M.S.); sandipswarnakar.2008@gmail.com or sswarnakar@kluniversity.in (S.S.)

Abstract

Malaria persists to pose a prominent global health challenge, retained as one of the leading vector-borne diseases responsible for substantial illness and fatality rate, predominantly in tropical and subtropical regions. In this manuscript, a photonic crystal fiber (PCF)-based surface plasmon resonance (SPR) biosensor with an internal sensing configuration is presented to sense malaria-parasitized red blood cells (RBCs). Sensor works by measuring the refractive index (RI) differences relative to healthy and malaria-affected RBCs at numerous developmental stages, including ring (R_P), trophozoite (T_P), and schizont (S_P). The optimized design shows different resonant wavelength (λ_{res}), shifts from 1319 nm for normal RBCs to 1242 nm, 1159 nm, and 1073 nm for the R_P, T_P, and S_P stages, respectively, allowing for accurate stage-wise discrimination. The sensing structure has utmost confinement loss (α_{cl}) of 19,066 dB/cm, wavelength sensitivity ($S_{wavelen}$) of 11,000 nm/RIU, amplitude sensitivity (S_{ampli}) of 55.98 RIU^{-1}, resolution (R_{es}) of 10^{-6} RIU, detection precision of 0.018, and largest Quality Factor (OF) of 84.82 RIU^{-1}. The large λ_{res} shift, high sensitivity, great spectrum selectivity, and superior sensing performance suggest that the proposed biosensor can accurately detect minute RI fluctuations associated with malaria infection. The internal sensor design improves the optical interaction among light and analyte, increasing sensing efficiency and stability. These properties make the proposed PCF-SPR biosensor a promising platform for quick, extremely sensitive, non-invasive, and label-free malaria diagnosis, with significant promise for future biomedical and point-of-care diagnostics.

Keywords: malaria detection; ring phase; wavelength sensitivity; internal sensing; surface plasmon resonance

Check for updates

Received: 3 September 2026
Revised: 12 October 2026
Accepted: 18 October 2026
Published: 21 October 2026

Copyright: © 2026 by the authors. Licensee MDPI, Basel, Switzerland. This article is an open access article distributed under the terms and conditions of the Creative Commons Attribution (CC BY) license.

1. Introduction

SPR optical sensors are crucial in biomedical applications as they detect biomolecules in real-time subject to their RI [1,2]. SPR-dependent sensors are being adopted for a diversity of applications, including temperature/pressure sensing [3,4], environmental monitoring, liquid level detection and food safety, and the SPR proceeding emerges when

light associates with a metal-dielectric (M-D). A p-polarized wave-based energy spreads throughout a dielectric core, while a surface plasmon wave (SPW) flows at the plasmonic interfacial region [5,6]. SPR analyses energy transfer-related spectral losses and P-polarized waves disrupt the (M-D) interaction as they go through the core. At the $\boldsymbol{\lambda_{res}}$, the propagation parameter (γ) of the resultant evanescent field corresponds to that of the SPW. The $\boldsymbol{\lambda_{res}}$, where the sensor experiences greatest dissipation, indicates the maximal sensitivity of the construction [5]. The sensor's greatest loss shows energy transfer to the (M-D) junction, which contributes to its high sensitivity [7].

Broad-spectrum RI sensors with great sensitivity are in considerable demand in the optoelectronic and biomedical industries [8,9]. Researchers have developed sensitive sensors to measure exterior RIs and sensors with different geometries, such as V-shaped, double-side-polished, D-shaped, and U-grooved have been constructed to identify a wide variety of RIs [8–13]. Although SPR sensors offer excellent sensitivity, their design complexity limits their use in extensive RI sensing. Microwave-based sensors with better sensitivity emerged as alternatives to SPR sensors that are used in bio-sensing applications.

However, their sophisticated setups and complexity limit their practical use [14,15]. Biomedical applications require high-sensitivity SPR sensors to detect external RI [16]. Fiber-optic-utilizing sensors are predominantly used because of their economically viable, stable, and excellent sensing performance. Silica glass alloyed with $\boldsymbol{GeO_2}$ is widely utilized as a core layer for guiding electromagnetic waves because of its affordability, high-temperature stability, and strong adhesion to metal interfaces used in sensor fabrication [17]. These properties make $\boldsymbol{GeO_2}$-doped silica a suitable choice for high-performance PCF-based biosensing applications. Researchers have used air hole geometries in silica cores to improve strength, sensitivity, and flexibility in sensor designs. The air pores in the core reduce loss and direct energy to the (M-D) contact, improving sensor response to external media [15].

The Kretschmann method is commonly used in sensors to create an M-D interface. This involves depositing a tiny coating of gold (Au) on a prism. Gold is chosen for its extensive porosity, functional stability, sensitive properties, and low volatility [18]. Silver (Ag) provides smaller resonance peaks and higher detection accuracy (DA), but has lesser stability [19]. Dielectric materials, including oxides, have been studied because oxide compounds with significant dielectric constant are ideal for holding electric fields. Materials like $\boldsymbol{SiO_2}$, $\boldsymbol{TiO_2}$, ITO, $\boldsymbol{Fe_2O_3}$ and ZnO have been coupled with metallic deposits to enhance sensor sensitivity [20–22]. The poor selectivity, sensitivity to specific gases of $\boldsymbol{Fe_2O_3}$ [23] reduce their effectiveness in sensor applications and $\boldsymbol{SiO_2}$ has a low RI detection range [22], while ITO is fragile, costly, sensitive to temperature, chemically reactive, and has limited flexibility [24]. ZnO and $\boldsymbol{TiO_2}$ have toxicological and photographic corrosion effects, prompting researchers to seek alternate oxide forms [25]. α-$\boldsymbol{Al_2O_3}$ has a high working function and strong adhesion active sensing region for bio-analysis, which makes it perfect for bio-sensing systems [26]. Thermal oxidation of aluminum allows for easy synthesis, lowering sensor fabrication costs and retaining stability [27]. α-$\boldsymbol{Al_2O_3}$ has gained popularity for its high economic feasibility, biocompatibility, dielectric constant, low dissolution tendency, and outstanding stability under thermodynamic equilibrium [28].

Malaria is a severe vector-borne contagious syndrome induced by protozoan protozoa of the Plasmodium genus and is carried to humans via the pierces of infected female Anopheles mosquitoes [29]. If left undiagnosed or inadequately treated, the infection can progress to severe malaria, leading to fatal complications such as cerebral malaria, multiple tissue dysfunction, coma, and death [30]. Following inoculation, Plasmodium sporozoites reach the liver, where they experience hepatic proliferation before emitting merozoites into the circulatory system. These merozoites subsequently infect RBCs, activating the

erythrocytic period of the parasite's biological mechanism, which induces the characteristic clinical manifestations including fever, fatigue, nausea, and headache [31].

Malaria parasites, commonly referred to as sporozoites, penetrate human cells and human tissues through mosquito bites [32]. Malaria comprises three stages, beginning with the ring phase ($\boldsymbol{R_P}$), where merozoites penetrate RBCs and change into mono-nucleated trophozoites. Trophozoites transform into schizonts, which are multinucleated cells [33]. Timely diagnosis is critical for dealing with affected patients and lowering mortality. Typically, diagnosis is based on clinical evaluation of patient signs, clinical features, and physical findings. A clinical diagnosis may be challenging since indications overlap with other common medical conditions [34,35]. Microscopically examining blood smears with field stains is a conventional way for diagnosing malaria, in contrast, it takes proficiency to avoid diagnostic inaccuracy if there is mixed illness or low parasitaemia [36]. The quantitative buffy coat (QBC) approach enhances micro-level detection by staining blood and employing epifluorescent microscopy. Nevertheless, it necessitates specialized techniques, costlier than light microscopy, and incapable of correctly estimating a parasite kind or count [37]. Rapid diagnostic tests (RDTs) identify microbial antibodies or enzymes in blood, providing a rapid and convenient approach. RDTs identify Plasmodium-specific antigens or enzymatic biomarkers in blood, providing a quick and easy alternative [32]. Serological approaches to identify antibodies towards malaria pathogen are adaptive but time-consuming and difficult to replicate, limiting daily sample output [38]. Loop-mediated isothermal amplification (LAMP) is a cost-effective and easier substitute to polymerase chain reaction (PCR) that detects turbidity during DNA amplification. Malaria diagnosis has been examined using microarrays, mass spectrometry (MS), flow cytometry (FCM) and automated blood cell counters (ABCC). However, the aforementioned methods need to be validated through clinical trials [39]. PCF has potential uses in sensors such as SPR, hydrostatic pressure, temperature, chemical, terahertz RI, and malaria detection [40–46].

This research proposes and models a ring-shaped SPR sensor in COMSOL Multiphysics 5.6 for detecting biological samples with different RIs. An affordable production technique for sensors has been presented. The proposed sensor has the improved sensor configuration for prompt diagnosis of malaria signs in humans. The sensor's response for malaria detection includes the $\boldsymbol{R_P}$, $\boldsymbol{T_P}$ and $\boldsymbol{S_P}$ with average RIs of 1.395, 1.383, and 1.373, respectively [47–51]. Referenced to normal RBCs with a RI 1.402 sensor exhibits high wavelength sensitivity ($\mathbf{S_{wavelen}}$) of 11,000, 8421.05, and 8482 nm/RIU for $\boldsymbol{R_P}$, $\boldsymbol{T_P}$, $\boldsymbol{S_P}$ RBCs, respectively.

The suggested sensor outperforms previous malaria sensors guided by on the SPR occurrence, as reported in [52–56]. This study represents a substantial development in sensing, especially for bio and optical sensors, due to its high sensitivity, DA, low cost, and flexibility of fabrication.

2. Design and Numerical Modeling of the Proposed Sensor

2.1. Geometrical Configuration and Structural Parameters

The proposed biosensor geometry is illustrated in Figure 1a, showing the transverse geometry of the designed PCF. Numerical modeling and optimization are accomplished using the finite element method (FEM) in COMSOL Multiphysics. The fiber core contains a centrally located elliptical sensing channel specified by a semi-major axis (a) and a semi-minor axis (b), as depicted in Figure 1b. The sensing channel is embedded by several films of circular air holes positioned in a hexagonally ordered configuration to achieve efficient light confinement and controlled propagation characteristics. The optimized structural configuration enhances the converged connecting the guided optical field and the biomarker, thereby producing improved SPR excitation and superior biosensing

performance. The proposed sensor structure features a cladding with circular air cavities in the core with two different radii (d_s and d_L) in a silica substrate that regulates the flow of light. The arrangements of the air cavities of these two different radii (r) are organized in a hexagonal shape with the values of the air cavities as d_s = 1.38 µm and d_L = 1.40 µm. The pitch (Λ), which is kept constant at 2 µm throughout the suggested sensor design, represents the inter-hole spacing between two neighboring air holes. The biosensor's modal confinement, effective RI, and phase-matching properties are all significantly influenced by pitch. A two-dimensional perfectly matched layer (PML) is further enclosing the PCF's outer boundary to precisely replicate the open-boundary circumstances. By efficiently absorbing electromagnetic waves that propagate outward, the PML removes false reflections from the computing domain, increasing the precision of the numerical analysis. The chosen PML thickness of 1 µm is adequate to provide effective absorption while preserving computational efficiency.

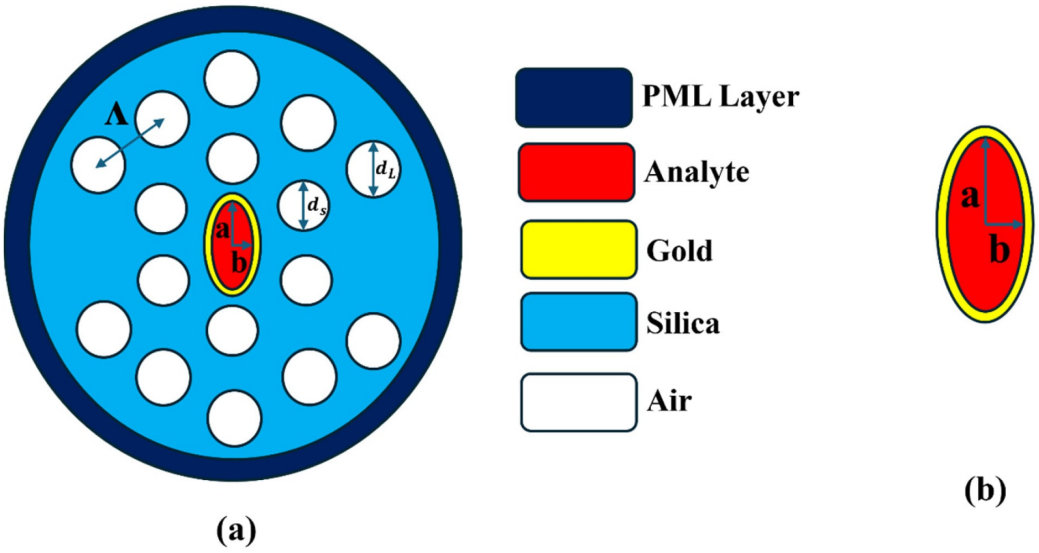


Figure 1. (**a**) The devised structure for malaria detection through internal sensing. (**b**) Elliptical sensing channel indicating semi-major axis and minor axis.

The eccentricity of the central elliptical channel can be expressed as Equation (1) [54]:

$$e = \sqrt{1 - \frac{b^2}{a^2}}, \text{ where } a > b \tag{1}$$

In this case, a and b stand for the center elliptical sensing channel's semi-major and semi-minor axes, correspondingly. Fused silica was choosedas the background material for the suggested biosensor because of its great chemical resistance, low intrinsic absorption, outstanding optical transparency, and superior thermal stability. For PCF-based biosensors functioning covering a diverse set spanning from ultraviolet (UV) to near-infrared (NIR) region, fused silica is a perfect substrate because of these features. Additionally, the Sellmeier equation found in Equation (2) [32] properly describes the wavelength-dependent dispersion of its RI. The RI may be precisely calculated over the operational wavelength range thanks to Table 1, which lists the matching Sellmeier coefficients utilized in the numerical simulations.

$$n^2(\lambda) = 1 + \frac{A_1\lambda^2}{\lambda^2 - B} + \frac{A_2\lambda^2}{\lambda^2 - B_2} + \frac{A_3\lambda^2}{\lambda^2 - B_3} \tag{2}$$

Table 1. Coefficients of Sellmeier equation.

Parameter	Value
n	Refractive Index
A1	0.69616
A2	0.407942
A3	0.897479
B1	4.679148×10^{-3} μm^2
B2	1.351206×10^{-2} μm^2
B3	97.93400 μm^2

The recommended sensor is designed with a gold [57] plasmonic material for effective sensing with the thickness ((t_{Au}) of 20 nm. By using gold nanowires in conjunction with the precise placement and sizes of the holes in the PCF design, the evanescent fields become more concentrated, providing ideal coupling properties that result in higher R_{es}, better sensitivities, and appropriate FOM values than other materials [58]. The sensor is designed for internal sensing, so the gold coating is encircled with elliptical sensing channel which serves as a sensing path in the core. The Drude–Lorentz model defines the wavelength-dependent RI $n(\lambda)$ of gold as Equation (3) [5] where $\epsilon_m(\lambda)$ represents wavelength-dependent complex electric permittivity of gold materials. The terms $n_m(\lambda)$ and $k_m(\lambda)$ refer to real and imaginary sections of gold's RI.

$$n(\lambda) = \sqrt{(\epsilon_m(\lambda))} = n_m(\lambda) + ik_m(\lambda) \tag{3}$$

$\epsilon_m(\lambda)$ is additionally specified below as Equation (4) [8], and all Drude–Lorentz attributes are further given in Table 2.

Table 2. Coefficients of Drude–Lorentz model.

Parameter	Value
ϵ_{Au} (Gold's permittivity)	-
ϵ_{a} (Permittivity at high frequency)	5.99673
ω (Angular Frequency)	$\frac{2\pi c}{\lambda}$
γ_D (Damping frequency)	1.0003×10^{14} rad/s
ω_D (Plasmon Frequency)	1.3280×10^{16} rad/s
$\frac{\gamma_D}{2\pi}$	15.92 THz
$\frac{\omega_D}{2\pi}$	2113.6 THz
Ω_L	650.07
$\frac{\Gamma_L}{2\pi}$	104.86 THz

$$\epsilon_{\mathrm{Au}} = \epsilon_{\mathrm{a}} - \frac{\omega_D^2}{\omega(\omega + j\gamma_D)} - \frac{\Delta\epsilon\,\Omega_L^2}{(\omega^2 - \Omega_L^2) + j\Gamma_L\omega} \tag{4}$$

Park et al. [48] studied RI values of infected and normal RBC in human system. Plasmodium falciparum, the malaria-causing parasite, exhibits varying RI values during its intra-erythrocytic phase. Table 3 shows the RIs of normal and parasitized RBCs throughout various phases of malaria parasite life cycle.

Table 3. Refractive indices of the normal and diseased red blood cells.

Various Development Phases of Malaria Infection	Refractive Index	References
Healthy Phase	1.402	[7,47]
Ring Phase	1.395	
Trophozoite Phase	1.383	
Schizont Phase	1.373	

2.2. Key Performance Indicators

The effective detecting of implemented SPR sensor is analyzed using essential performance metrics, including resonance wavelength, $\boldsymbol{\alpha_{cl}}$, $\mathbf{S_{wavelen}}$, $\mathbf{S_{ampli}}$, $\boldsymbol{R_{es}}$, FWHM, detection accuracy (DA), and FOM. These parameters quantify the sensor's capacity to analyze microscopic RI alterations with high sensitivity and accuracy.

2.2.1. Confinement Loss

The $\boldsymbol{\alpha_{cl}}$ for core mode transmission in PCF-SPR sensors is referred as Equation (5) [8]:

$$\boldsymbol{\alpha_{cl}}(\mathbf{dB/cm}) = \frac{2\pi f}{c} \times \mathbf{8.686} \times \boldsymbol{Im}\left(\boldsymbol{n_{eff}}\right)(\mathrm{dB/cm}) \quad (5)$$

where $\boldsymbol{Im}(\boldsymbol{n_{eff}})$ corresponds to imaginary component of the effective RI of fundamental mode, (f) is the frequency of incident optical wave and (c) is speed of light in free space.

2.2.2. Wavelength Sensitivity

The $\mathbf{S_{wavelen}}$ of designed PCF-SPR biosensor is determined from $\boldsymbol{\lambda_{res}}$ shift induced by changes in the analyte RI ($\Delta \boldsymbol{RI}$). A larger $\boldsymbol{\lambda_{res}}$ shift for a given RI variation indicates higher sensing performance. The $\mathbf{S_{wavelen}}$ is calculated using Equation (6) [8].

$$\mathbf{S_{wavelen}}(\mathbf{nm/RIU}) = \frac{\Delta \boldsymbol{\lambda_p}}{\Delta \mathbf{n}} \quad (6)$$

2.2.3. Amplitude Sensitivity

The amplitude sensitivity has been formulated as in Equation (7) [8]

$$\mathbf{S_{ampli}}\left(\mathbf{RIU}^{-1}\right) = -\frac{1}{\boldsymbol{\alpha_{cl}}} \frac{\Delta \boldsymbol{\alpha_{cl}}}{\Delta \mathbf{n}} \quad (7)$$

In this equation, $\boldsymbol{\alpha_{cl}}$ describes confinement loss for a certain RI unit used to measure sensor's flow. $\boldsymbol{\alpha_{cl}}$ and n represent the difference in $\boldsymbol{\alpha_{cl}}$ and RI between two cells with different RI values. By monitoring the change in $\boldsymbol{\alpha_{cl}}$ and RI unit, the biological sensor's ability to discriminate among normal and infected cells was evaluated.

2.2.4. Resolution

Sensor $\boldsymbol{R_{es}}$ refers to an SPR sensor's capacity to observe even little changes in the RI of detecting cell. Variations in the RI of sample cell can be identified by examining variations in $\boldsymbol{R_{es}}$ of the established design which is illustrated in Equation (8) [8].

$$\mathbf{RI}(\mathbf{RIU}) = \frac{\Delta \boldsymbol{n} \times \Delta \boldsymbol{\lambda_{min}}}{\Delta \boldsymbol{\lambda_p}} \quad (8)$$

The minimal wavelength shift, $\boldsymbol{\lambda_{min}}$, is defined as 1 nm.

2.2.5. Full-Width Half Maximum and Detection Accuracy

It is described as the α_{cl} curve's spectral width at half of its highest value. The interval separating the lower and upper cutoff wavelengths which corresponds to 70.7% ($1/\sqrt{2}$) of the maximum α_{cl}, is used to determine the FWHM. A narrower resonance peak is indicated by a reduced FWHM, which improves sensing performance and spectral R_{es}. A lower FWHM results in improved detection accuracy since DA and FWHM are negatively correlated. Equation (9) is used to calculate the FWHM [8].

$$\mathbf{DA}(\mu\mathbf{m}^{-1}) = \frac{1}{FWHM} \tag{9}$$

2.2.6. Quality Factor (QF) or Figure of Merit (FOM)

One of the most important factors for biosensor is quality factor can also refer as Figure of Merit (FOM). It is determined as percentage of sensitivity to FWHM [56], and the following is how, it is expressed in Equation (10).

$$\mathbf{QF}\ (\mathbf{or})\ \mathbf{FOM} = \frac{\mathbf{S}}{\mathbf{FWHM}}\mathbf{RIU}^{-1} \tag{10}$$

3. Performance Outcomes of the Proposed Sensor

3.1. Sensing Mechanism of the Presented Biosensor

The sensing mechanism is governed by the phase-matching condition between the core-guided fundamental mode and the surface plasmon polariton (SPP) mode supported at the gold-analyte interface, which occurs when the real parts of their effective mode indices are equal; at this wavelength, energy couples resonantly from the core mode to the SPP mode, resulting in the observed loss peak. Malaria infection causes a decrease in analyte RI due to the parasite (Plasmodium) consuming and degrading intracellular hemoglobin, a dense, high-RI biomolecule. This lowers the effective biomolecular concentration inside the RBC, and because the RI scales with the density/concentration of dissolved biomolecules in a medium, the RBC refractive index gradually decreases with infection stage, corresponding to light traveling faster through the parasitized cell than through a healthy, hemoglobin-rich RBC. This decreasing analyte RI lowers the effective index of the SPP mode, because SPP dispersion is directly proportional to the adjacent dielectric index, shifting the phase-matching wavelength to a shorter value relative to the core-mode dispersion curve and producing the observed blue shift; conversely, a higher RBC RI (healthy or early-stage cell) raises the SPP effective index and red-shifts the resonance.

The SPR [59,60] mechanism is developed in the M-D contact by supporting a p-polarized electromagnetic pulse. The significant absorption of light resulted from an optical energy propagation amid incident and reflected light energy. The γ for SPW is defined as in Equation (11) [5].

$$\beta_{SPW} = \beta_0 \sqrt{\frac{\epsilon_{mr}.n_s^2}{\epsilon_{mr} + n_s^2}} \tag{11}$$

where $\beta_0 = 2\pi/\lambda$, ϵ_{mr} is M-D constant, and n_s is sensing (dielectric) layer's RI. As a result, changes in RI cause varied fluctuation-induced phase mismatch in light path, leading to very robust SPR sensors and its propagation mode is determined by the optical energy confinement enclosed in the core and at the M-D interface. SPR sensors can operate in three modes: core, coupling, and SPP. Figure 2a presents distribution of electric field for the Y-polarized core mode at λ_{res} (1319 nm), as well as a 3-D representation on the right. Figure 2b depicts electric field dispersion of confined optical mode at the λ_{res} representing the coupling mode. At this wavelength, high coupling efficiency occurs among core and the SPP mode, causing optical field to be distributed almost equally across the fiber core

and the M-D interface. This balanced field distribution confirms strong plasmonic coupling and effective exchange of optical power to SPP mode. Figure 2c highlights SPP mode of sensor for the λ_{res} 1319 nm. Maximum α_{cl} at λ_{res} corresponding to SPP mode, where the optical field is predominantly localized at the M-D interface, indicating efficient stimulation of surface plasmons.

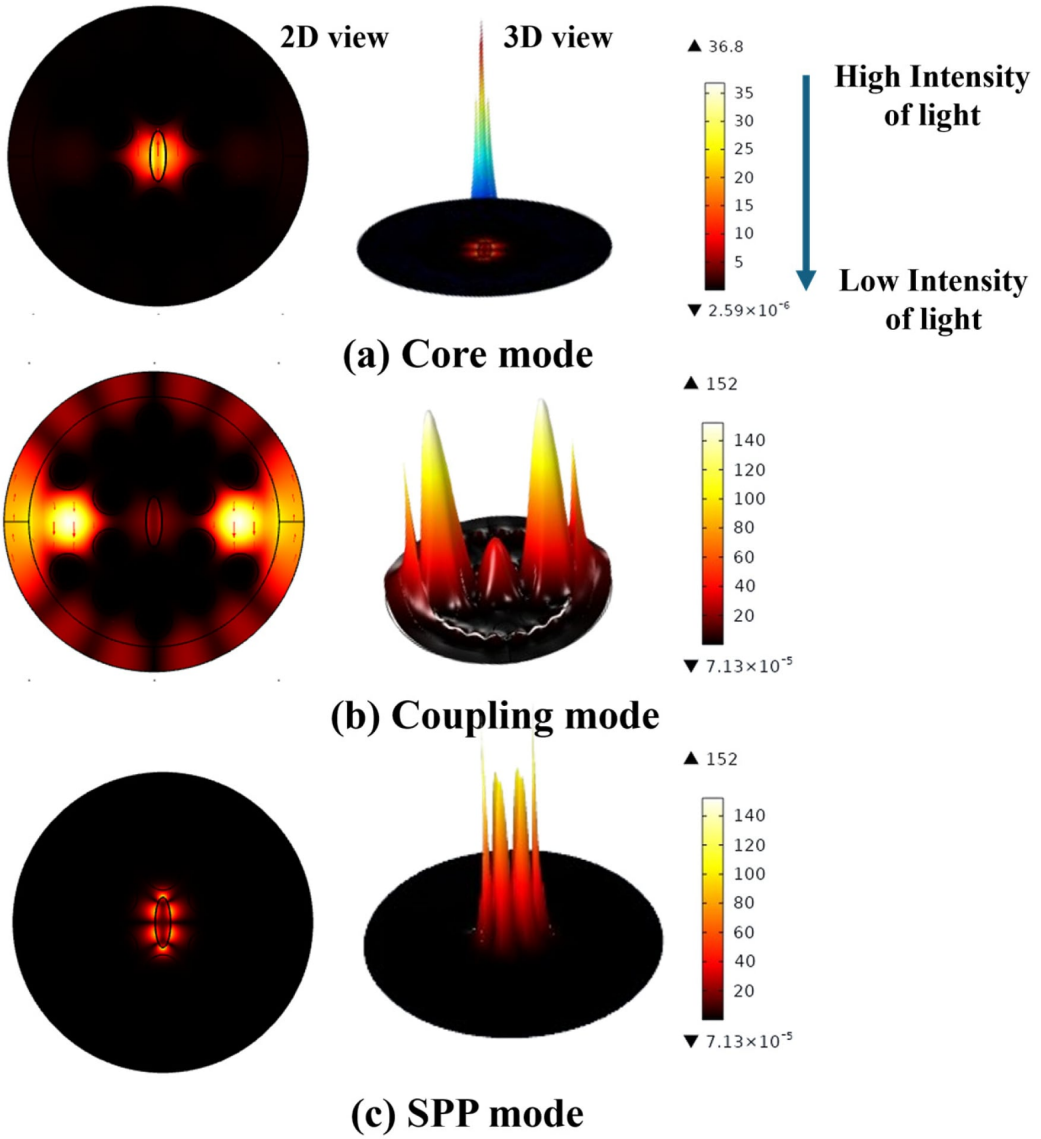


Figure 2. Electric intensity distribution of the Y-polarized mode showing the 2D, 3D electric field, and its intensity for the (**a**) core mode, (**b**) coupling mode, and (**c**) surface plasmon polariton (SPP) mode, respectively.

The formulation of coupled modes explains how fields of electricity are partitioned and what means mode interaction occurs in SPR-based PCFs. The relations illustrating mode coupling are as given in Equations (12) and (13) [12]:

$$\frac{dE_1}{dz} = i\beta_1 E_1 + iKE_2 \tag{12}$$

$$\frac{dE_2}{dz} = i\beta_2 E_2 + iKE_1 \tag{13}$$

The high order γ for core and SPP modes are β_1 and β_2, correspondingly. The electric fields for the core and SPP modes are E_1 and E_2, respectively. The coupling intensity and

propagation length are represented by E_1 and E_2. In the phase mating situation, actual components of β_1 and β_2 are equivalent, causing the core to couple with the SPP mode.

A metal-coated analyte interface supports plasmonic modes, which in turn interact with the basic core mode in the suggested PCF biosensor. The third-order SPP mode was chosen from the examined plasmonic modes due to its favorable resonance properties and electric-field distribution [13]. The increased interaction between the analyte and the evanescent optical field is enabled by this higher-order mode, which displays a clear field distribution with substantial localization around the metal-analyte interface. There is an efficient transfer of energy from the core-guided mode to the plasmonic mode when phase matching happens, which happens when the real part of the effective refractive index of the fundamental core mode approaches that of the third-order SPP mode. The resonance frequency is matched by a distinctive peak in the confinement-loss spectrum, which is caused by this coupling. Changes in the phase-matching condition, which causes changes in the resonance wavelength, are caused by fluctuations in the analyte refractive index that are linked with different stages of malaria infection. So, to test the resonance response and wavelength sensitivity of the suggested sensor for label-free malaria detection, the third-order SPP mode is used.

3.2. Analysis of Malaria Detection

This section examines the applicability of the design for malaria detection. The finite element method (FEM) simulations were carried out in COMSOL Multiphysics with a tetrahedral mesh, consisting of 76 vertex elements, 1055 boundary elements, and 19,213 total elements, with a minimum element quality of 0.4551 to ensure that the mesh was free of highly distorted or degenerate elements that could compromise solution accuracy. This mesh density was chosen after a convergence analysis. The resonance positions and loss values remained steady during additional refinement, indicating that the presented results are numerically convergent and independent of the discretization utilized. The device's parameters were tuned to detect normal and contaminated RBCs. The RI of normal and infected RBCs was retrieved using the practical approach described by Park et al. [48]. Cells with precise RI were inserted and accurate evaluation of malaria in the human body is confirmed by shift in $\lambda_{\mathbf{res}}$ and amplitude of α_{cl}.

The α_{cl} was calculated by tracking the appropriate guided mode across the wavelength range at a 1 nm step. The loss spectra show significant changes due to the high coupling between the guided core mode and the SPP mode approaching the phase-matching condition. The α_{cl} spectra for the core mode of normal sample with RI (1.402) show a maximum α_{cl} of 9770.5 dB/cm at the λ_{res} of 1319 nm. In infected R_p cells with RI (1.395), the SPP and core modes cross at 1242 nm λ_{res} with a α_{cl} of 13,599 dB/cm. The R_p cell exhibits a 77 nm shift in λ_{res} with respect to normal cell for a RI change of 0.007, demonstrating device's excellent sensitivity. Sensor detects a $\lambda_{\mathbf{res}}$ of 1159 nm in T_p RBCs with a RI of 1.383, which is 160 nm lower than in normal phase. The α_{cl} for the T_p is presented to be 15,197 dB/cm. Finally, S_p RBCs had a $\lambda_{\mathbf{res}}$ of 1073 nm when referenced to normal cells, indicating the detector's best sensitivity. The α_{cl} amplitude for the S_p was determined to be 19,066 dB/cm. The reported shift in RI for T_p and S_p RBCs are 0.019 and 0.029, respectively. Figure 3 depicts the loss spectra as well as effective RI variation curves of Y-polarized fundamental core and SPP mode for four different RBC conditions corresponding to malaria progression: (a) normal phase (RI = 1.402), (b) R_p (RI = 1.395), (c) T_p (RI = 1.383), and (d) S_p (RI = 1.373). The effective RI of core mode steadily drops as wavelength enhances, whereas the SPP mode has a distinct dispersion behavior due to its high dependency on the plasmonic interface. The convergence of these two dispersion curves reflects the phase-matching condition, in which optical power is optimally coupled from core to SPP mode.

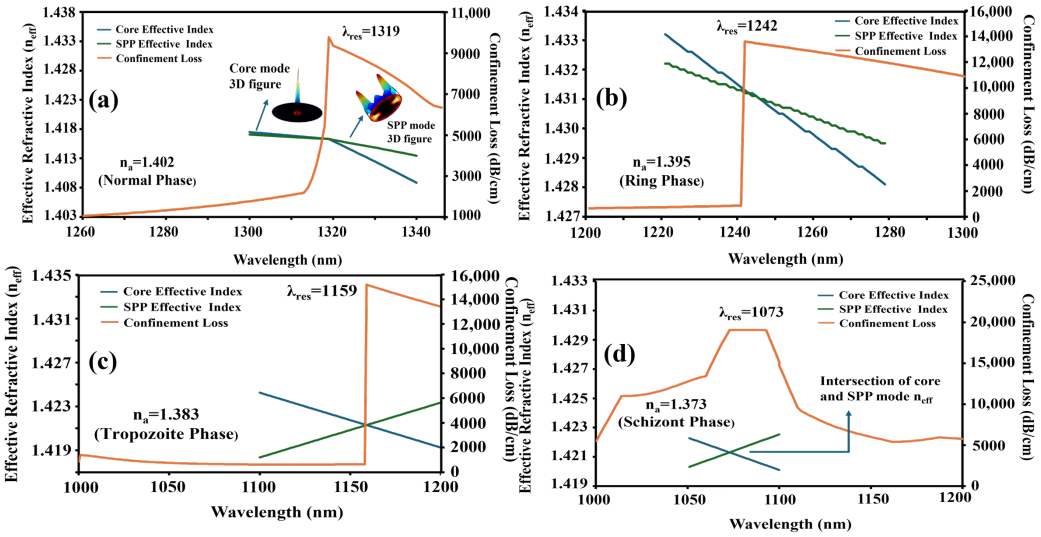


Figure 3. Attenuation curves for Y polarized mode in relation with the wavelengths for effective index of core and SPP modes (**a**) normal phase (RI-1.402) (**b**) ring phase (RI-1.395) (**c**) trophozoite phase (RI-1.383) (**d**) schizont phase (RI-1.373).

Figure 4 displays changes in the core of n_{eff}, SPP n_{eff}, and λ_{res} across healthy, R_P, T_P, and S_P blood samples. The core n_{eff} gradually declines with increasing wavelength in all four examples, whereas the SPP n_{eff} exhibits an opposite dispersion tendency, resulting in the two curves converging at a certain wavelength. The crossing point varies between blood samples, demonstrating that each malaria stage has a distinct optical reaction. The S_P has the initial contact at 1073 nm, followed by the healthy phase at 1319 nm, T_P at 1159 nm, and R_P at 1242 nm. These λ_{res} are obviously distinct from one another, indicating a unique spectral response for each stage of malaria infection. Furthermore, the α_{cl} curves for each sample show clear peaks at these wavelengths, with maximum values of 19,066 dB/cm, 9770.5 dB/cm, 15,197 dB/cm, and 13,599 dB/cm for S_P, healthy, T_P, and R_P, respectively. The n_{eff} curves are smooth over the wavelength range studied, demonstrating consistent modal propagation characteristics. The considerable shift in resonance frequency across blood samples reflects differences in the optical functionalities of healthy and diseased RBCs. Furthermore, the distinct separation between the resonance sites minimizes ambiguity in determining the appropriate malaria stage, increasing the dependability of the suggested biosensor. The image also shows that each blood sample has a distinct spectral signature, allowing for easy differentiation between healthy, R_P, T_P, S_P phases. It should be highlighted that this study is purely based on numerical simulation, with no actual fibers manufactured or experimentally tested. The reported confinement loss values (~9770–19,066 dB/cm) are caused by strong core-to-plasmon mode coupling at resonance and serve as a spectroscopic figure-of-merit for identifying the resonance wavelength, rather than representing a loss that a real signal must propagate through over long distances. Using the standard relation L = 4.343/α, these values correspond to a characteristic interaction length of ~2–4 μm. In practice, sensing relies on wavelength-interrogation—tracking the shift of the resonance/loss peak with analyte refractive index—rather than transmission-based detection through the lossy region, so the high loss does not prevent experimental measurement. Indeed, this high loss is beneficial in the present context, as it produces a sharp, high-contrast resonance dip that improves sensitivity and detectability, at the cost of a short usable interaction length. Realizing this design experimentally would require attention to this short interaction length, and further optimization of the metal layer thickness or fiber geometry could help tailor the loss to practical fabrication requirements, which we identify as a direction for future work and can be further extended by using

machine and deep learning [61]. The well-defined resonance locations and precise spacing between successive resonance wavelengths demonstrate the proposed sensor's good selectivity for stage-wise malaria detection, making it suited for accurate and dependable biomedical diagnostic applications.

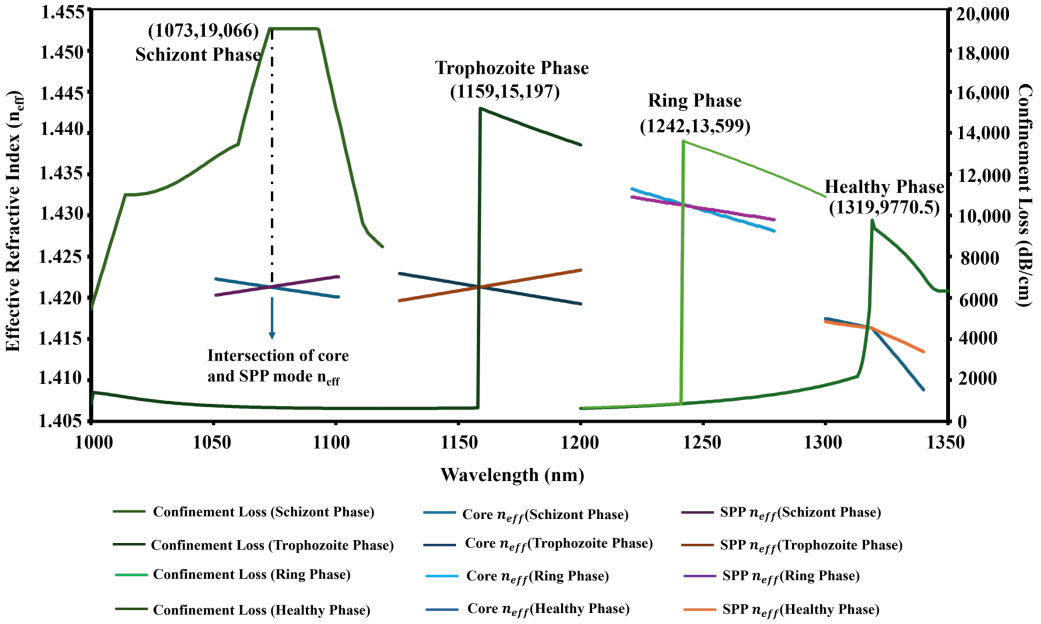


Figure 4. Resonance shift for the change in refractive indices for healthy, ring, trophozoite and schizont phases.

Table 4 summarizes sensing performance of designed PCF biosensor in identifying normal and malaria-infected RBCs at three developmental stages: $\boldsymbol{R_P}$, $\boldsymbol{T_P}$, $\boldsymbol{S_P}$. The $\boldsymbol{\lambda_{res}}$ gradually drops from 1319 nm for normal RBC to 1242 nm, 1159 nm, and 1073 nm for the $\boldsymbol{R_P}$, $\boldsymbol{T_P}$, $\boldsymbol{S_P}$. respectively, revealing a noticeable blue shift as the RBC's RI decreases throughout malaria progression. The significant difference between the $\boldsymbol{\lambda_{res}}$ allows for accurate differentiation of each infection stage without spectral overlap. The $\boldsymbol{\alpha_{cl}}$ increases from 9770.5 dB/cm in the normal sample to 19,066 dB/cm in the $\boldsymbol{S_P}$, indicating a stronger contact within the optical and the sensing region. Higher $\boldsymbol{\alpha_{cl}}$ causes a more noticeable resonance peak, which improves signal visibility and aids in correct detection. The designed sensor has a extreme $\mathbf{S_{wavelen}}$ of 11,000 nm/RIU for the $\boldsymbol{R_P}$, while the $\boldsymbol{T_P}$ and $\boldsymbol{S_P}$ have sensitivities of 8421.05 nm/RIU and 8482 nm/RIU. These high sensitivity results show that even little RI fluctuations induced by malaria infection result in considerable $\boldsymbol{\lambda_{res}}$ shifts, making the sensor appropriate for early detection. The $\boldsymbol{R_P}$ has the highest $\boldsymbol{S_{ampli}}$ (55.98 RIU^{-1}), followed by the $\boldsymbol{T_P}$ (29.23 RIU^{-1}) and $\boldsymbol{S_P}$ (32.8 RIU^{-1}) stages, indicating strong intensity-based sensing capability. The biosensor's $\boldsymbol{R_{es}}$ values are in the order of 10^{-6} RIU, showing its capacity to analyze minor RI changes with precision. The FWHM values of 53 nm, 158 nm, 141 nm, and 100 nm suggest strong spectral characteristics, with narrower resonance peaks improving spectral selectivity and reducing uncertainty in determining the $\boldsymbol{\lambda_{res}}$. The DA values of 0.018, 0.0063, 0.007, and 0.01 show that resonance peaks may be identified with high precision, especially for the $\boldsymbol{S_P}$ due to its shorter linewidth. The suggested biosensor's good sensing performance is confirmed by FOM values of 69.62 RIU^{-1}, 59.72 RIU^{-1}, and 84.82 RIU^{-1}. The $\boldsymbol{S_P}$ has the highest FOM due to its favorable balance between sensitivity and resonance linewidth. Overall, the performance metrics show that the proposed PCF biosensor has high sensitivity, outstanding $\boldsymbol{R_{es}}$, strong optical coupling, robust spectral selectivity, and consistent stage-specific discriminating capabilities. These properties make the sensor a promising platform for fast, label-free, highly

accurate optical sensing of RI variations in biomedical applications. Although the proposed structure has been investigated numerically, its practical realization requires consideration of the fabrication [62] of the internal elliptical sensing channel and the deposition of the internal Au layer. In principle, the PCF preform can be fabricated using a stack-and-draw approach, in which suitably shaped capillaries are arranged to form the central elliptical channel and surrounding air-hole structure. After fiber drawing, the internal sensing surface could potentially be coated with Au using an appropriate internal deposition or coating process to obtain a nominal thickness of approximately 20 nm. The internal channel could subsequently be connected to a suitable fluidic interface for introducing the analyte or biological sample. However, achieving a uniform Au thickness over the complete internal elliptical surface and maintaining the designed channel dimensions may be challenging. Deviations in channel dimensions, ellipticity, pitch, or Au thickness can modify the guided-mode/SPP coupling condition and shift the resonance response. Therefore, the present simulations represent the ideal geometrical and material conditions, and the fabrication tolerance of the proposed structure has not been experimentally established. Experimental fabrication, dimensional-tolerance analysis, Au-coating characterization, controlled analyte filling, and biological-sample testing are required to verify the practical performance of the proposed sensor.

Table 4. Performance parameters obtained for proposed sensor.

Parameter	Normal RBC	R_p	T_p	S_p
Resonance peak (nm)	1319	1242	1159	1073
Confinement loss (dB/cm)	9770.5	13,599	15,197	19,066
Wavelength Sensitivity (nm/RIU)	-	11,000	8421.05	8482
Amplitude Sensitivity (RIU^{-1})	-	55.98	29.23	32.8
Resolution (RIU)	-	0.9×10^{-6}	0.07×10^{-6}	0.047×10^{-5}
FWHM (nm)	53	158	141	100
Detection Accuracy	0.018	0.0063	0.007	0.01
Figure of Merit (RIU^{-1})	-	69.62	59.72	84.82

4. Optimization of Functional Parameters

Numerous geometrical characteristics have a substantial impact on sensor performance. Phase-complementing points can be arranged in many ways by varying constraints such as pitch, air cavity diameters and t_{Au}. These variables are essential in determining how well the sensor system performs, affecting both its sensitivity and general operation. By carefully adjusting these geometrical characteristics, the sensing capabilities can be adjusted to satisfy particular needs and maximize performance in the sensing application.

4.1. Influence of Diameter of Air Cavity Variation on Sensitivity

4.1.1. Impact of Small Hole Diameter (d_S)

The suggested PCF biosensor's sensing characteristics were evaluated by systematically adjusting the d_S value from 1.34 µm to 1.48 µm to assess structural tolerance and performance stability. The normal sample has λ_{res} covering from 1150 nm to 1164 nm, whereas the R_P varies from 1151 nm to 1161 nm. The T_P exhibits resonance wavelengths varying from 1073 nm to 1092 nm, but the S_P is practically constant at 933–934 nm, showing re-

markable phase-matching stability. The $\boldsymbol{\alpha_{cl}}$ also varies little with $\boldsymbol{d_S}$, ranging from 3410.8 to 4551 dB/cm for the normal sample, 3060.9–3772.5 dB/cm for the $\boldsymbol{R_P}$, 7664.8–8266.2 dB/cm for the $\boldsymbol{T_P}$, and 14,652–14,752 dB/cm for the $\boldsymbol{S_P}$, confirming that the plasmonic coupling strength is largely preserved across the investigated design range. The $\boldsymbol{S_{wavelen}}$ peaks at 1714 nm/RIU for the $\boldsymbol{R_P}$, 5000 nm/RIU for the $\boldsymbol{T_P}$, and 7965 nm/RIU for the $\boldsymbol{S_P}$, indicating improved RI discrimination for advanced malaria stages. Similarly, the $\boldsymbol{S_{ampli,}}$ varies from 0.028 to 46.02 $\boldsymbol{RIU^{-1}}$ for the $\boldsymbol{R_P}$, 37.31–74.92 RIU^{-1} for the $\boldsymbol{T_P}$, and 77.29–113.65 RIU^{-1} for the $\boldsymbol{S_P}$. The $\boldsymbol{S_P}$ has the highest response due to higher modal interaction during resonance. Overall, the small fluctuations in $\boldsymbol{\lambda_{res}}$, $\boldsymbol{\alpha_{cl}}$, $\boldsymbol{S_{wavelen}}$ and $\boldsymbol{S_{ampli,}}$ demonstrate that the proposed PCF biosensor has high geometric tolerance, stable phase-matching properties, and consistent sensing performance at 1.38 µm, making it suitable for practical fabrication and highly reliable malaria diagnosis. All parameters like $\boldsymbol{\lambda_{res}}$, $\boldsymbol{\alpha_{cl}}$, $\boldsymbol{S_{wavelen}}$ and $\boldsymbol{S_{ampli}}$ obtained with respect to variation in $\boldsymbol{d_S}$ is tabulated in Table 5 and the respective graphs are depicted in Figure 5.

Table 5. Response of small air hole diameter on the optical performance of the proposed PCF biosensor.

Value of d_S	Parameter	Normal RBC	R_P	$T_{P,}$	S_P
1.34	S_{ampli} (RIU^{-1})	-	15.15	74.92	113.65
	$S_{wavelen}$ (nm/RIU)	-	571.42	4263	7586
	α_{cl} (dB/cm)	3410.8	3772.5	8266.2	14,652
	λ_{res} (nm)	1154	1158	1073	934
1.36	S_{ampli} (RIU^{-1})	-	11.85	61.41	99.03
	$S_{wavelen}$ (nm/RIU)	-	1571	4000	7448
	α_{cl} (dB/cm)	3784.4	3470.4	8200	14,652
	λ_{res} (nm)	1150	1161	1074	934
1.38	S_{ampli} (RIU^{-1})	-	32.05	41.83	78.21
	$S_{wavelen}$ (nm/RIU)	-	428.57	5000	7931.03
	α_{cl} (dB/cm)	4513.5	3519.9	8102.4	14,752
	λ_{res} (nm)	1163	1160	1078	933
1.40	S_{ampli} (RIU^{-1})	-	29.83	41.09	78.21
	$S_{wavelen}$ (nm/RIU)	-	428.57	4882.35	7931.03
	α_{cl} (dB/cm)	4513.9	3571.3	8037.9	14,752
	λ_{res} (nm)	1163	1160	1080	933
1.42	S_{ampli} (RIU^{-1})	-	28.24	39.96	78.2
	$S_{wavelen}$ (nm/RIU)	-	571.42	4210.52	7931.03
	α_{cl} (dB/cm)	4514.3	3621.8	7942.4	14,752
	λ_{res} (nm)	1163	1159	1083	933
1.44	S_{ampli} (RIU^{-1})	-	46.02	39.2	78.12
	$S_{wavelen}$ (nm/RIU)	-	1714	4105	7931
	α_{cl} (dB/cm)	4515.9	3060.9	7879.4	14,752
	λ_{res} (nm)	1163	1151	1085	933

Table 5. *Cont.*

Value of d_S	Parameter	Normal RBC	R_P	T_P,	S_P
1.46	S_{ampli} (RIU^{-1})	-	34.98	37.31	77.29
	$S_{wavelen}$ (nm/RIU)	-	428.57	4052.63	7965
	α_{cl} (dB/cm)	4551	3436.7	7817.3	14,752
	λ_{res} (nm)	1164	1161	1087	933
1.48	S_{ampli} (RIU^{-1})	-	0.028	63.59	110.92
	$S_{wavelen}$ (nm/RIU)	-	1000	3315	7586
	α_{cl} (dB/cm)	3498.3	3499.9	7725	14,752
	λ_{res} (nm)	1153	1160	1090	933

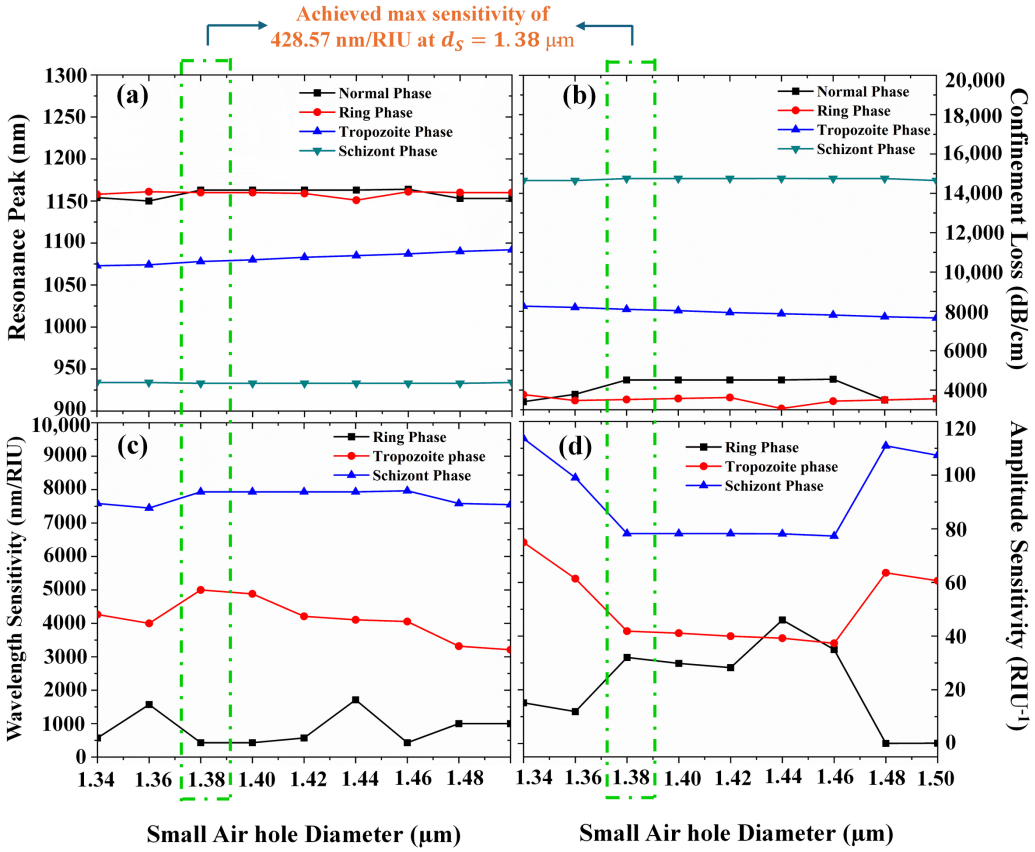


Figure 5. Variation in the sensing characteristics of the suggested PCF biosensor with small air hole diameter (**a**) resonance wavelength, (**b**) confinement loss, (**c**) wavelength sensitivity, and (**d**) amplitude sensitivity.

4.1.2. Impact of Large Air Hole Diameter (d_L)

The PCF-SPR biosensor's sensing performance was tested with d_L ranging from 1.34 µm to 1.48 µm. The electromagnetic field distribution is strongly perturbed, resulting in a large λ_{res} shift at d_L = 1.40 µm. The λ_{res} fluctuates between 1149 and 1186 nm, 1151–1170 nm, 1082–1155 nm, and 931–1039 nm for the normal, R_P, T_P, and S_P, respectively. As d_L grows, the λ_{res} varies just slightly between 1.34 µm and 1.48 µm, suggesting robust phase matching and great fabrication tolerance. The optimized diameter of 1.44 µm results in α_{cl} of 3893.9 dB/cm, 3594.6 dB/cm, 8061.1 dB/cm, and 14,980 dB/cm for the normal, R_P, T_P, and S_P respectively, indicating effective plasmonic mode excitation. The α_{cl} is relatively stable across the optimized diameter range, indicating strong optical confinement and reliable plasmonic coupling. Furthermore, the optimized structure achieves

$S_{wavelen}$ of 1285 nm/RIU, 3473 nm/RIU, and 7482 nm/RIU for the, T_P, and S_P, respectively. The optimized diameter yields S_{ampli} of 10.97 RIU^{-1}, 59.33 RIU^{-1}, and 98.18 RIU^{-1} for each malaria stage. The increased S_{ampli} reported for advanced malaria stages confirms enhanced plasmonic resonance and a greater optical field overlap with the sensor region. The minimal fluctuation in λ_{res}, α_{cl}, and sensitivity within the optimized diameter range reveals remarkable structural robustness to fabrication-induced dimensional variations. The optimal air-hole diameter strikes a balance between optical confinement, resonance strength, and RI discrimination while ensuring sensor stability. These findings suggest that d_L = 1.40 µm offers the best balance of sensitivity, loss, resonance stability, and manufacturing tolerance. As a result, the chosen air-hole diameter assures that the proposed biosensor detects different phases of malaria infection reliably and efficiently. All parameters like λ_{res}, α_{cl}, $S_{wavelen}$, and S_{ampli} obtained with respect to variation in d_L is tabulated in Table 6 and the respective graphs are illustrated in Figure 6.

Table 6. Effect of large air hole diameter proceeding optical performance of the designed PCF biosensor.

Value of d_L	Parameter	Normal RBC	R_P	T_P	S_P
1.34	S_{ampli} (RIU^{-1})	-	8.66	29.81	103.37
	$S_{wavelen}$ (nm/RIU)	-	1428	3315	7517
	α_{cl} (dB/cm)	3594	3376	7558	14,368
	λ_{res} (nm)	1153	1163	1090	935
1.36	S_{ampli} (RIU^{-1})	-	0.612	51.45	101.28
	$S_{wavelen}$ (nm/RIU)	-	1142	3315	7482
	α_{cl} (dB/cm)	3664	3649	7247	14,427
	λ_{res} (nm)	1152	1160	1089	935
1.38	S_{ampli} (RIU^{-1})	-	26.56	39.55	78.61
	$S_{wavelen}$ (nm/RIU)	-	571.42	4105.26	7931
	α_{cl} (dB/cm)	4448	3622	3649	3376
	λ_{res} (nm)	1164	1160	1086	934
1.40	S_{ampli} (RIU^{-1})	-	46.02	39.2	78.12
	$S_{wavelen}$ (nm/RIU)	-	1714	4105	7931
	α_{cl} (dB/cm)	4515.9	3060.9	7879.4	14,752
	λ_{res} (nm)	1163	1151	1085	933
1.42	S_{ampli} (RIU^{-1})	-	2.74	69.75	105.04
	$S_{wavelen}$ (nm/RIU)	-	1285	3473	7482
	α_{cl} (dB/cm)	3662	3595	8509	14,815
	λ_{res} (nm)	1150	1159	1084	933
1.44	S_{ampli} (RIU^{-1})	-	10.97	59.33	98.18
	$S_{wavelen}$ (nm/RIU)	-	1285	3473	7482
	α_{cl} (dB/cm)	3893.9	3594.6	8061.1	14,980
	λ_{res} (nm)	1149	1158	1083	932

Table 6. *Cont.*

Value of d_L	Parameter	Normal RBC	R_P	T_P	S_P
1.46	S_{ampli} (RIU^{-1})	-	34.12	36.34	73.08
	$S_{wavelen}$ (nm/RIU)	-	714.28	4210	7931
	α_{cl} (dB/cm)	4824	3672	8155	15,047
	λ_{res} (nm)	1162	1157	1082	932
1.48	S_{ampli} (RIU^{-1})	-	44.86	35.39	75.26
	$S_{wavelen}$ (nm/RIU)	-	285.71	4157.89	7931
	α_{cl} (dB/cm)	4915	3371	8220	15,214
	λ_{res} (nm)	1161	1159	1082	931

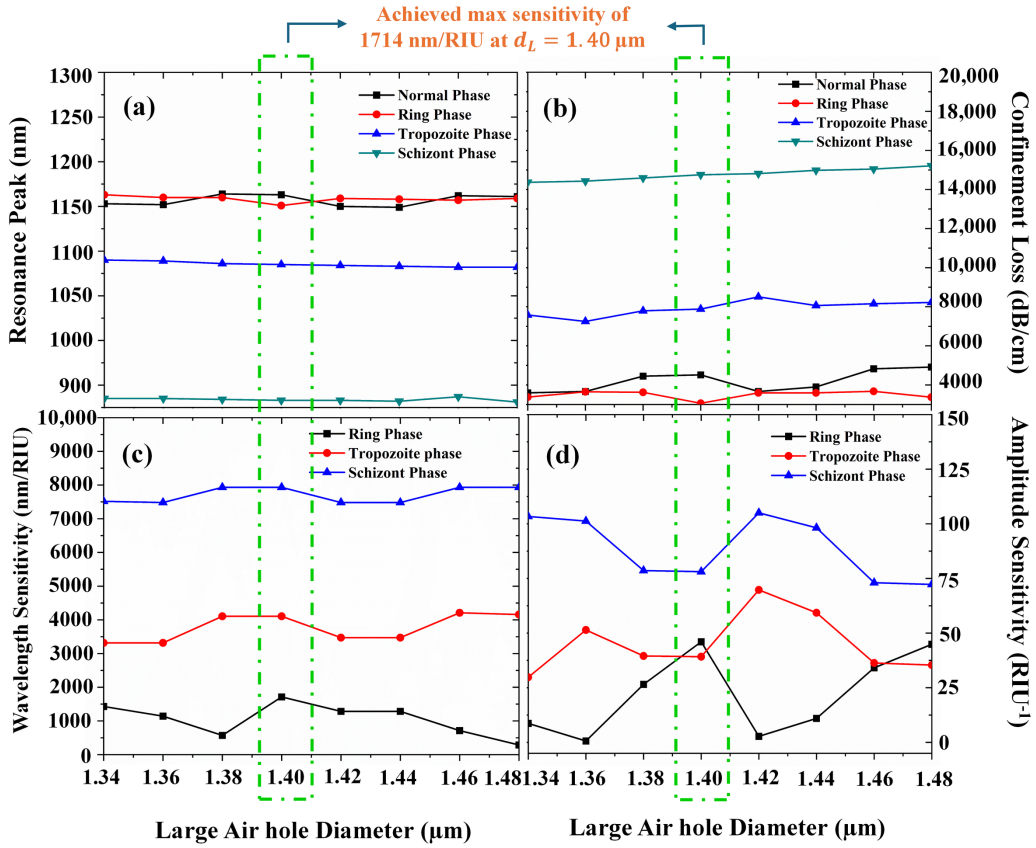


Figure 6. Variation in the sensing characteristics of designed PCF biosensor with the large air hole diameter (**a**) resonance wavelength, (**b**) confinement loss, (**c**) wavelength sensitivity, and (**d**) amplitude sensitivity.

4.2. Response of Gold Layer Thickness Value (t_{Au})

The effect of altering structural parameter like gold layer thickness (t_{Au}) on sensing capability of the mentioned PCF biosensor was thoroughly examined, with t_{Au} reduced from 34 nm to 18 nm. As t_{Au} drops, the normal and R_P samples show a significant red shift in λ_{res}, with maximum values of 1319 nm and 1242 nm, respectively, at t_{Au} = 20 nm, indicating improved optical confinement and greater modal coupling. The T_P and S_P show an overall red shift with slight fluctuations caused by changes in effective RI matching and modal overlap. The α_{cl} increases significantly for all analytes, reaching peak values of 9770.5 dB/cm (normal), 13,599 dB/cm (R_P), 15,197 dB/cm (T_P), and 19,066 dB/cm (S_P) at t_{Au} = 20, demonstrating enhanced energy pass from guided to sensing mode. Intensity-based sensitivity. The $S_{wavelen}$, likewise increases dramatically as t_{Au} decreases,

reaching 11,000 nm/RIU for the R_P at t_{Au} = 20, while the T_P and S_P approach optimum sensitivities of 8947.36 nm/RIU and 8862.06 nm/RIU, respectively, at t_{Au} = 22. In contrast, S_{ampli} exhibits its maximum values at intermediate t_{Au} values, with peak sensitivities of 85 RIU^{-1} (R_P), 96.14 RIU^{-1} (T_P), and 99.98 RIU^{-1} (S_P). This suggests that excessive modal coupling beyond the optimum point slightly broadens the resonance spectrum and reduces intensity-based sensitivity. At t_{Au} = 18, no resonance peak or guided core mode is recorded for any analyte, indicating that the structural geometry no longer meets the phase-matching criterion needed for stable mode propagation. These findings show that t_{Au} efficiently controls light-matter interaction, modal confinement, and plasmonic coupling efficiency in the sensing region. Taking all performance metrics into account, t_{Au} = 20 is the best structural configuration for numerical identification/discrimination of the modeled RBC states using the proposed PCF biosensor, ensuring strong resonance characteristics, maximum loss, high wavelength sensitivity, and robust overall sensing performance. All parameters like λ_{res}, α_{cl}, $S_{wavelen,}$, and S_{ampli} obtained with respect to variation in t_{Au} is tabulated in Table 7 and the respective graphs are depicted in Figure 7.

Table 7. Effect of gold layer thickness on optical performance of the designed PCF biosensor.

Value of t_{Au}	Parameter	Normal RBC	R_P	T_P	S_P
18	S_{ampli} (RIU^{-1})	-	-	-	-
	$S_{wavelen}$ (nm/RIU)	-	11,000	No modes	No modes
	α_{cl} (dB/cm)	-	-	-	-
	λ_{res} (nm)	-	-	-	-
20	S_{ampli} (RIU^{-1})	-	55.98	29.23	32.8
	$S_{wavelen}$ (nm/RIU)	-	11,000	8421.05	8482
	α_{cl} (dB/cm)	9770.5	13,599	15,197	19,066
	λ_{res} (nm)	1319	1242	1159	1073
22	S_{ampli} (RIU^{-1})	-	85	59.57	61.09
	$S_{wavelen}$ (nm/RIU)	-	7285.71	8947.36	8862.06
	α_{cl} (dB/cm)	6520.4	10,400	13,901	18,073
	λ_{res} (nm)	1290	1239	1120	1033
24	S_{ampli} (RIU^{-1})	-	77.34	78.53	80.5
	$S_{wavelen}$ (nm/RIU)	-	3714.28	8631.57	8655.17
	α_{cl} (dB/cm)	5163.5	7958.6	12,868	17,218
	λ_{res} (nm)	1251	1225	1087	1000
26	S_{ampli} (RIU^{-1})	-	62.72	96.14	98.69
	$S_{wavelen}$ (nm/RIU)	-	1714.28	8263.15	8379.31
	α_{cl} (dB/cm)	4247.2	6112	12,005	16,402
	λ_{res} (nm)	1216	1204	1059	973
28	S_{ampli} (RIU^{-1})	-	22.81	79.65	99.98
	$S_{wavelen}$ (nm/RIU)	-	142.85	6157.89	7896
	α_{cl} (dB/cm)	3970.2	4604.3	9978.5	15,482
	λ_{res} (nm)	1181	1182	1064	952

Table 7. *Cont.*

Value of t_{Au}	Parameter	Normal RBC	R_P	T_P	S_P
30	S_{ampli} (RIU^{-1})	-	32.05	41.83	78.21
	$S_{wavelen}$ (nm/RIU)	-	428.57	5000	7931.03
	α_{cl} (dB/cm)	4513.5	3519.9	8102.4	14,752
	λ_{res} (nm)	1163	1160	1078	933
32	S_{ampli} (RIU^{-1})	-	31.61	29.72	46.9
	$S_{wavelen}$ (nm/RIU)	-	428.57	2631	5137
	α_{cl} (dB/cm)	4370.8	3403.8	6839.2	10,316
	λ_{res} (nm)	1136	1133	1086	987
34	S_{ampli} (RIU^{-1})	-	7.31	31.17	60.37
	$S_{wavelen}$ (nm/RIU)	-	1571.42	368.42	4310.03
	α_{cl} (dB/cm)	3561.1	3378.9	5670.2	9795.6
	λ_{res} (nm)	1097	1108	1090	972

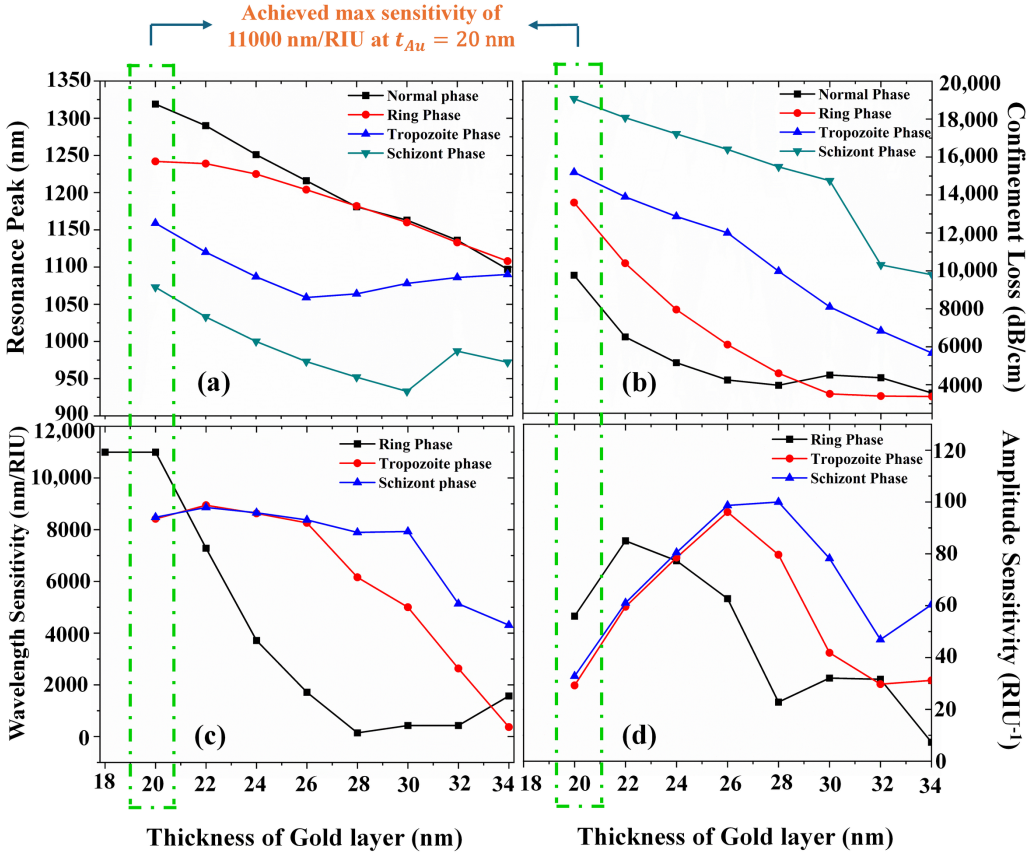


Figure 7. Change in sensing characteristics of the proposed PCF biosensor with respect to gold layer thickness (**a**) resonance wavelength, (**b**) confinement loss, (**c**) wavelength sensitivity, and (**d**) amplitude sensitivity.

4.3. Influence of Elliptical Sensing Channel

4.3.1. Impact of Major Axis of Elliptical Sensing Channel (a)

The effect of elliptical sensing channel semi-major axis (a) on the sensing specifications of the PCF biosensor was analyzed by altering a from 0.6 to 1.2 µm. The results show that the semi-major axis has a substantial effect on the phase-matching condition, effective RI distribution, and modal binding across guided core mode and sensing mode,

changing $\boldsymbol{\lambda_{res}}$, $\boldsymbol{\alpha_{cl}}$, $\boldsymbol{S_{wavelen,}}$, and $\boldsymbol{S_{ampli}}$. As 'a' increases from 0.6 µm to the optimized value of 1.0 µm, all analytes exhibit a pronounced red shift in $\boldsymbol{\lambda_{res}}$, reaching maximum values of 1319 nm (normal), 1242 nm ($\boldsymbol{R_P}$), 1159 nm ($\boldsymbol{T_P}$), and 1073 nm ($\boldsymbol{S_P}$). This indicates enhanced evanescent-field interaction and stronger plasmonic coupling. The $\boldsymbol{\alpha_{cl}}$ also varies significantly along the semi-major axis, where the optimized geometry provides well-defined resonance characteristics with $\boldsymbol{\alpha_{cl}}$ of 9770.5 dB/cm, 13,599 dB/cm, 15,197 dB/cm, and 19,066 dB/cm for the normal, $\boldsymbol{R_P}$, $\boldsymbol{T_P}$, and $\boldsymbol{S_P}$ samples, respectively, confirming efficient energy transfer between interacting modes. At da = 1.0 µm, the $\boldsymbol{S_{wavelen}}$ peaks at 11,000 nm/RIU for the $\boldsymbol{R_P}$, 8421.05 nm/RIU for the $\boldsymbol{T_P}$, and 8482 nm/RIU for the $\boldsymbol{S_P}$, indicating enhanced RI detection capacity. Smaller (0.6 µm) and bigger (1.2 µm) semi-major axes significantly diminish $\boldsymbol{S_{wavelen}}$ due to poor phase matching and altered modal field distribution. The $\boldsymbol{R_P}$ has the highest $\boldsymbol{S_{ampli}}$ of 135.17 RIU^{-1} at 'a' = 0.8 µm, while the $\boldsymbol{S_P}$ has an exceptional high value of 842.05 RIU^{-1} at a = 1.2 µm. This suggests that intensity-based sensing is more affected by resonance depth than wavelength shift. However, these standalone advantages are accompanied by less desirable resonance and wavelength sensitivity properties. The optimum semi-major axis for malaria identification using the constructed biosensor is 'a' = 1.0 µm, which offers the best balance of strong resonance characteristics, efficient plasmonic coupling, high $\boldsymbol{S_{wavelen}}$, stable mode propagation, and overall superior sensing performance. All parameters like $\boldsymbol{\lambda_{res}}$, $\boldsymbol{\alpha_{cl}}$, $\boldsymbol{S_{wavelen}}$ and $\boldsymbol{S_{ampli}}$ obtained with respect to variation in a is tabulated in Table 8 and the respective graphs are depicted in Figure 8.

Table 8. Influence of major axis of elliptical sensing channel on the optical presentation of the proposed PCF biosensor.

Value of Major Axis (a)	Parameter	Normal RBC	$\boldsymbol{R_P}$	$\boldsymbol{T_P}$	$\boldsymbol{S_P}$
0.6	S_{ampli} (RIU^{-1})	-	0.041	2.04	1.13
	$S_{wavelen}$ (nm/RIU)	-	285.71	315.78	310.34
	α_{cl} (dB/cm)	17,166	17,161	17,834	17,731
	λ_{res} (nm)	1024	1022	1018	1015
0.8	S_{ampli} (RIU^{-1})	-	135.17	0.318	0.4
	$S_{wavelen}$ (nm/RIU)	-	6285.71	473.68	448.27
	α_{cl} (dB/cm)	16,340	878.35	16241	16,150
	λ_{res} (nm)	1103	1059	1094	1090
1	S_{ampli} (RIU^{-1})	-	55.98	29.23	32.8
	$S_{wavelen}$ (nm/RIU)	-	11,000	8421.05	8482
	α_{cl} (dB/cm)	9770.5	13,599	15,197	19,066
	λ_{res} (nm)	1319	1242	1159	1073
1.2	S_{ampli} (RIU^{-1})	-	8.8	10.34	842.05
	$S_{wavelen}$ (nm/RIU)	-	285.71	210.52	2413.79
	α_{cl} (dB/cm)	715.81	760.15	856.44	18,180
	λ_{res} (nm)	1075	1073	1071	1145

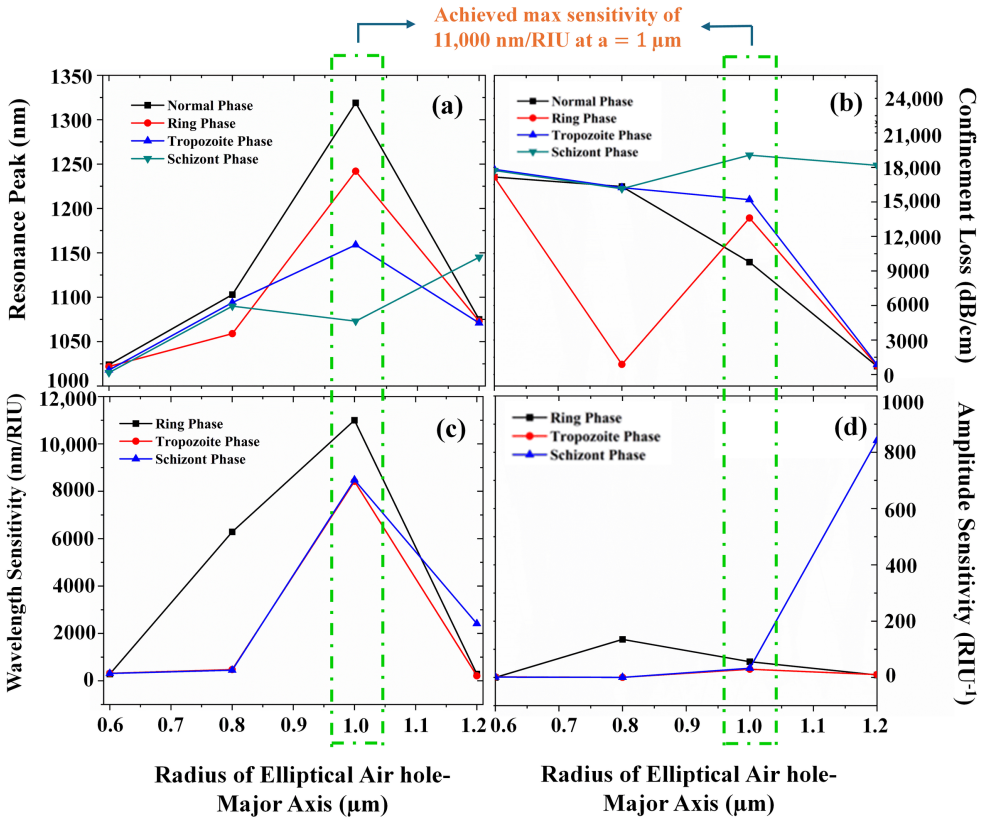


Figure 8. Variation in the sensing characteristics of the implemented PCF biosensor with major axis of elliptical sensing channel (**a**) resonance wavelength, (**b**) confinement loss, (**c**) wavelength sensitivity, and (**d**) amplitude sensitivity.

4.3.2. Impact of Minor Axis of Elliptical Sensing Channel (b)

The suggested PCF biosensor's performance was evaluated by altering the semi-minor axis of elliptical sensing channel (b) from 0.1 µm to 0.5 µm. The findings show that b regulates the effective RI distribution, optical field confinement, modal overlap, and phase-matching between the guided core and sensing mode, all of which have a significant impact on the λ_{res}, α_{cl}, $S_{wavelen}$ and S_{ampli}. As the semi-minor axis increases from 0.1 µm to the optimized value of 0.3 µm, all analytes exhibit a significant red shift in λ_{res}, reaching 1319 nm (normal), 1242 nm (R_P), 1159 nm (T_P), and 1073 nm (S_P), indicating enhanced evanescent-field interaction and efficient plasmonic coupling. The α_{cl} increases from 833.66 to 865.49 dB/cm at b = 0.1 µm to 9770.5 dB/cm, 13,599 dB/cm, 15,197 dB/cm, and 19,066 dB/cm for the analytes at b = 0.3 µm, indicating enhanced energy transfer from guided to sensing modes. Increasing the semi-minor axis to 0.5 µm results in substantial α_{cl} and a blue shift in λ_{res}. This indicates degradation of phase-matching due to over-coupling and increased optical leakage. At b = 0.3 µm, the $S_{wavelen}$ reaches maximum values of 11,000 nm/RIU, 8421.05 nm/RIU, and 8482 nm/RIU for the R_P, T_P, , and S_P, respectively. This demonstrates good RI detection capacity. In contrast, both smaller (0.1 µm) and larger (0.5 µm) semi-minor axes considerably lower $S_{wavelen}$, due to inadequate or excessive modal interaction. The optimized geometry results in the maximum S_{ampli} values of 55.98 RIU^{-1}, 29.23 RIU^{-1}, and 32.8 RIU^{-1} for the R_P, T_P and S_P respectively. Other semi-minor axis values show significant reductions. These results demonstrate that the semi-minor axis effectively controls the light-matter interaction, resonance depth, and plasmonic coupling efficiency in the sensing region. The optimal structural parameter for malaria identification using the designed PCF biosensor is b = 0.3 µm, which balances resonance characteristics, loss, wavelength and amplitude sensitivity, stable mode propagation, and overall sensing performance. All parameters like λ_{res}, α_{cl}, $S_{wavelen}$, and S_{ampli}, obtained with

respect to variation in b is tabulated in Table 9 and the respective graphs are depicted in Figure 9. The elliptical geometry of the sensing channel further modifies the spatial field distribution and polarization-dependent confinement of the core mode, increasing its overlap with the analyte-filled channel and the adjacent gold layer along the major axis, which enhances modal overlap and coupling strength. The pitch (Λ) governs the background effective index and core-mode confinement by controlling air-hole spacing, thereby shifting the core-mode dispersion curve and, in turn, the phase-matching wavelength. The gold layer thickness controls SPP damping and coupling strength: thinner films increase field penetration and coupling, producing a sharper, more sensitive resonance, while thicker films suppress coupling and broaden or weaken the resonance. Collectively, these structural parameters tune the relative dispersion of the core and SPP modes, shifting the phase-matching wavelength and coupling strength, which directly determines both the resonance position (sensitivity) and the sharpness/depth of the loss peak (figure-of-merit). In this way, the biological stage of malaria infection is translated into a measurable, stage-dependent blue shift through the structure → field distribution → phase-matching → resonance-shift → sensitivity chain.

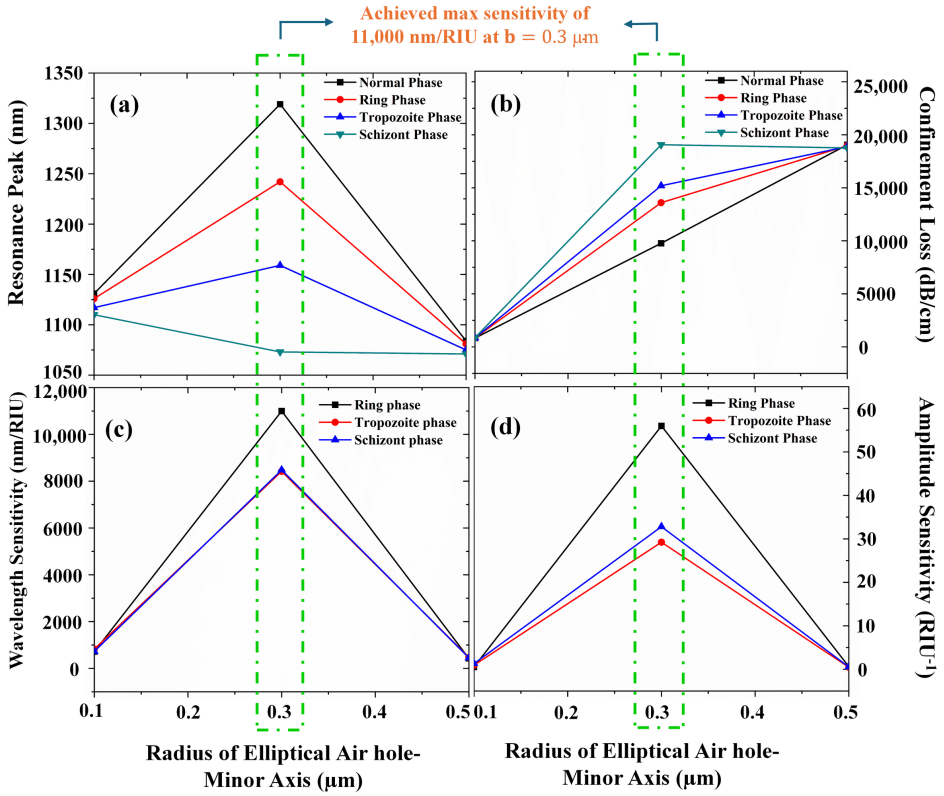


Figure 9. Variation in the sensing characteristics of the designed PCF biosensor with respect to the minor axis of Elliptical sensing channel (**a**) resonance wavelength, (**b**) confinement loss (**c**) wavelength sensitivity, and (**d**) amplitude sensitivity.

Table 9. Influence of minor axis of elliptical sensing channel on the optical performance of Proposed PCF biosensor.

Value of Minor Axis (b)	Parameter	Normal RBC	R_P	T_P	S_P
0.1	S_{ampli} (RIU^{-1})	-	0.54	0.95	1.31
	$S_{wavelen}$ (nm/RIU)	-	714.28	823.52	724.13
	α_{cl} (dB/cm)	833.66	836.81	848.74	865.49
	λ_{res} (nm)	1131	1126	1117	1110

Table 9. *Cont.*

Value of Minor Axis (b)	Parameter	Normal RBC	R_P	T_P	S_P
0.3	S_{ampli} (RIU^{-1})	-	55.98	29.23	32.8
	$S_{wavelen}$ (nm/RIU)	-	11,000	8421.05	8482
	α_{cl} (dB/cm)	9770.5	13,599	15,197	19,066
	λ_{res} (nm)	1319	1242	1159	1073
0.5	S_{ampli} (RIU^{-1})	-	0.629	0.46	0.53
	$S_{wavelen}$ (nm/RIU)	-	428.57	473.68	448.27
	α_{cl} (dB/cm)	19,057	18,973	18,888	18,759
	λ_{res} (nm)	1084	1081	1075	1071

5. Discussions of the Proposed Biosensor

A crucial component of the suggested PCF-SPR biosensor is the addition of a 20 nm Au layer inside the sensing channel, which adds a plasmonic sensing mechanism that is essentially different from traditional PCF RI sensors based on silica or Zeonex. As shown by the reported PCF RI sensors [51,53], sensing in traditional dielectric PCFs is mainly controlled by the interplay between the guided optical mode and the analyte-induced variation in effective RI. While Zeonex/polymer-based PCFs have also been studied for RI sensing in the THz regime, silica offers a low-loss dielectric platform [52,54]. Nevertheless, the free-electron response needed for traditional SPR is not inherent in these dielectric materials. The Au layer in the suggested structure creates a metal-dielectric interface that sustains a SPP, allowing the core-guided mode and the plasmonic mode to couple. Because the analyte is placed right next to the Au layer, variations in its RI alter the phase-matching condition and disturb the local plasmonic field, resulting in a detectable shift in resonance and variation in $\boldsymbol{\alpha_{cl}}$. Thus, rather than operating solely as a structural coating, the Au layer provides an additional plasmonic degree of freedom to improve the interaction between the guided light field and the analyte. This internal Au-analyte interface sets the proposed sensor apart from non-SPR silica PCF [51,53] and Zeonex/polymer-based THz PCF setups [52,54].

The numerical results show that the RI variation associated with the various malaria-infected RBC stages causes distinct modal responses. The resonance wavelengths of 1319, 1242, 1159, and 1073 nm observed for the normal RBC, $\boldsymbol{R_P}$, $\boldsymbol{T_P}$ and $\boldsymbol{S_P}$ conditions, respectively, can be attributable to differences in the phase-matching condition between the basic core-guided mode and the SPP. The decrease in analyte RI from 1.402 for normal RBC to 1.373 for the $\boldsymbol{S_P}$ alters the effective index of the plasmonic mode, shifting the resonance toward shorter wavelengths. The obtained $\boldsymbol{\lambda_{res}}$ exhibit distinct optical responses for the different cellular conditions considered within the 700–1500 nm operating range. This response agrees with the fundamental principle of PCF-based RI sensing reported in [51,53], where variations in the analyte RI lead to corresponding changes in the resonance characteristics. In the proposed sensor, the incorporation of an internal 20 nm Au layer further introduces plasmonic coupling at the analyte–metal interface. Consequently, changes in the analyte RI affect not only the propagation characteristics of the guided mode but also the coupling condition between the guided mode and the SPP mode. This combined interaction results in distinct resonance shifts for the different cellular stages. Hence, the obtained stage-dependent $\boldsymbol{\lambda_{res}}$ provide a numerical basis for distinguishing the considered malaria stages using the proposed PCF-SPR sensor.

The comparison presented in Table 10 indicates that the proposed sensor should be evaluated using multiple sensing parameters rather than $\boldsymbol{S_{wavelen}}$ alone. The design op-

erates in the near-infrared spectral band (700–1500 nm), is compatible with commonly accessible optical components, and improves practicality for real-time biosensing applications. The calculated $S_{wavelen}$ for the $\mathbf{R_P}$, $\mathbf{T_P}$ and $\mathbf{S_P}$ are 11,000, 8421.05, and 8482 nm/RIU, respectively, compared with 11,428.57, 9473.68, and 9655.17 nm/RIU reported for the elliptical PCF in [53] and 3571, 3158, and 3103 nm/RIU for the conventional PCF RI sensor in [51]. Although the proposed structure does not exhibit the highest $S_{wavelen}$ among the compared sensors, its internal SPR configuration with the Au layer provides additional sensing characteristics, including S_{ampli} of 55.98, 29.23, and 32.8 RIU^{-1}, resolutions of 0.9×10^{-6}, 0.07×10^{-6}, and 0.047×10^{-5} RIU, FWHM values of 158, 141, and 100 nm, and FOM values of 69.62, 59.72, and 84.82 RIU^{-1} for the $\mathbf{R_P}$, $\mathbf{T_P}$ and $\mathbf{S_P}$ respectively. These parameters provide complementary information on the resonance shift, intensity variation, detection resolution, spectral linewidth, and overall sensing response. Moreover, the reported sensors in [51–54] employ different materials, structural configurations, sensing mechanisms, and operating spectral regions; for example, the THz PCF in [52] combines internal RI sensing with machine-learning analysis, while the Zeonex/polymer-based PCF in [54] operates in the 0.5–2.5 THz range. Therefore, direct comparison of absolute sensitivity values between these THz sensors and the proposed NIR PCF-SPR sensor should be interpreted cautiously, as differences in operating regime, host material, modal-field distribution, and sensing mechanism can substantially influence the reported performance. Accordingly, Table 10 provides a comparative assessment of the reported sensing characteristics while accounting for the differences among the respective sensor configurations.

The obtained results should be interpreted in the context of the limitations of the numerical model adopted in this study. The reported sensing characteristics are calculated using predefined RI values corresponding to the considered RBC and malaria stages and therefore demonstrate the numerical feasibility of RI-based sensing rather than experimentally validated diagnostic performance. The proposed sensor employs silica-based optical guidance with an internal 20 nm Au layer to introduce plasmonic interaction, while the reference silica and Zeonex/polymer PCF sensors reported in [51–54] use different structural configurations and sensing mechanisms. In a practical implementation, variations in the actual cellular RI, Au-film thickness and uniformity, sensing-channel dimensions, analyte filling, and modal excitation conditions may affect the λ_{res}, linewidth, and confinement loss. In particular, fabrication of a uniform Au coating along the internal elliptical sensing channel and effective introduction of the analyte into the sensing region would require suitable fabrication and filling techniques. Experimental fabrication and optical characterization using malaria-infected blood samples are therefore required to verify the predicted spectral responses. Moreover, the present numerical investigation does not establish clinical sensitivity, specificity, or classification accuracy. Hence, the proposed design should be considered a numerically investigated internal PCF-SPR platform in which silica-based waveguiding and Au-mediated plasmonic interaction enable RI-dependent differentiation of the considered malaria stages, with experimental and clinical validation required to establish its practical diagnostic applicability. Furthermore, while most previous studies focus primarily on RI detection, the suggested sensor can identify multiple malaria infection phases based on minute RI alterations using a single internal sensing platform. The integration of an internal SPR architecture, near-infrared operation, comprehensive multi-parameter performance evaluation, and stage-specific malaria classification is the main novelty of the current work, providing a balanced combination of high sensitivity, excellent detection accuracy, and practical feasibility for next-generation label-free optical malaria diagnostics.

Table 10. Performance comparison of the proposed internal PCF-SPR biosensor with reported PCF-based malaria biosensors.

Sensor Type	SPR	Material Used	Detection Technique	Operating Wavelength Range	$S_{wavelen}$ ($\frac{nm}{RIU}$)	S_{ampli} (RIU^{-1})	R_{es} (RIU)	FWHM (nm)	DA	FOM (RIU^{-1})	Ref.
PCF RI	No	Silica	Internal RI	1.2–2.6 um	R_P: 3571; T_P: 3158; S_P: 3103	NR	NR	NR	NR	NR	[51]
Hollow-core PCF	No	Silica	Internal RI + ML	THz	Relative sensitivity ~97%	NR	NR	NR	NR	NR	[52]
Elliptical PCF	No	Silica	Internal RI	Near-IR	R_P: 11,428.57, T_P: 9473.68, S_P: 9655.17	NR	NR	NR	NR	NR	[53]
THz PCF	No	Zeonex/ Polymer	Internal THz RI	0.5–2.5 THz	R_P: 1,200,000, T_P: 1,115,263.15 S_P: 11,13,793. (X-pol) R_P: 1,050,000 T_P: 1,054,736.84 S_P: 10,32,758.62 (Y-Pol)	NR	NR	NR	NR	NR	[54]
Internal PCF-SPR	Yes	Au	Internal SPR	700–1500 nm	R_P: 11,000, T_P: 8421.05, S_P: 8482	R_P: 55.98, T_P: 29.23, S_P: 32.8	R_P: 0.9×10^{-6} T_P: 0.07×10^{-6} S_P: 0.047×10^{-5}	R_P: 158 T_P: 141 S_P: 100	R_P: 0.0063 T_P: 0.007 S_P: 0.01	R_P: 69.62 T_P: 59.72 S_P: 84.82	Present Work

6. Conclusions

A high-performance internal sensing PCF-SPR biosensor was successfully constructed and numerically tested for detecting malaria-infected RBCs at various phases of infection. The optimized sensor shows effective interaction between directed core and SPP modes, leading to unique $\boldsymbol{\lambda_{res}}$ for normal, $\boldsymbol{R_P}$, $\boldsymbol{T_P}$ and $\boldsymbol{S_P}$ RBC samples. The acquired $\boldsymbol{\lambda_{res}}$ of 1319 nm, 1242 nm, 1159 nm, and 1073 nm convincingly distinguish the various stages of malaria infection, proving the efficiency of suggested sensing method. The biosensor attains robust sensing performance, with a maximum $\boldsymbol{\alpha_{cl}}$ of 19,066 dB/cm, $\boldsymbol{S_{wavelen}}$ of 11,000 nm/RIU, $\boldsymbol{S_{ampli}}$ of 55.98 RIU^{-1}, $\boldsymbol{R_{es}}$ in the order of 10^{-6} RIU, DA of 0.018, and a maximum FOM of 84.82 RIU^{-1}. The high $\boldsymbol{S_{wavelen}}$ and low detection limit allow for the detection of minute RI changes associated with malaria advancement, while the narrow resonance features increase measurement precision and stage differentiation. Furthermore, the internal sensing design improves light-analyte interaction, resulting in stable plasmonic coupling and higher sensor reliability when compared to standard external sensing systems. The suggested design combines compactness, label-free operation, fast response, and excellent diagnostic accuracy, making it an appealing candidate for biomedical sensing applications. Future work will focus on the fabrication of the proposed structure, experimental validation, integration with microfluidic platforms, and the application of the sensing principle to multiplex detection of other blood-borne diseases, allowing for a portable and real-time point-of-care diagnostic system.

Author Contributions: Conceptualization, N.H. and S.S.; methodology, N.H. and M.J.M.; software, M.S.; validation, M.S., H.M. and S.S.; formal analysis, N.H. and M.J.M.; investigation, N.H. and H.M.; resources, M.S. and S.S.; data curation, H.M. and M.J.M.; writing—original draft preparation, N.H. and S.S.; writing—review and editing, M.S. and S.S.; visualization, S.S.; supervision, S.S.; project administration, S.S. and M.S., Funding acquisition, M.J.M. and M.S. All authors have read and agreed to the published version of the manuscript.

Funding: This research received no external funding.

Data Availability Statement: Dataset available on request from the authors.

Conflicts of Interest: The authors declare no conflict of interest.

References

1. Panda, A.; Pukhrambam, P.D. Modeling of high-performance SPR refractive index sensor employing novel 2D materials for detection of malaria pathogens. *IEEE Trans. Nanobiosci.* **2022**, *21*, 312–319. [CrossRef] [PubMed]
2. Nguyen, H.H.; Park, J.; Kang, S.; Kim, M. Surface plasmon resonance: A versatile technique for biosensor applications. *Sensors* **2015**, *15*, 10481–10510. [CrossRef] [PubMed]
3. Heidarzadeh, H. Highly sensitive plasmonic sensor based on ring shape nanoparticles for the detection of ethanol and D-glucose concentration. *IEEE Trans. Nanotechnol.* **2020**, *19*, 397–404. [CrossRef]
4. Zhou, J.; Qi, Q.; Wang, C.; Qian, Y.; Liu, G.; Wang, Y.; Fu, L. Surface plasmon resonance (SPR) biosensors for food allergen detection in food matrices. *Biosens. Bioelectron.* **2019**, *142*, 111449. [CrossRef] [PubMed]
5. Kadhim, R.A.; Yuan, L.; Xu, H.; Wu, J.; Wang, Z. Highly sensitive D-shaped optical fiber surface plasmon resonance refractive index sensor based on Ag-a-Fe_2O_3 grating. *IEEE Sens. J.* **2020**, *20*, 9816–9824. [CrossRef]
6. Prabowo, B.; Purwidyantri, A.; Liu, K.-C. Surface plasmon resonance optical sensor: A review on light source technology. *Biosensors* **2018**, *8*, 80. [CrossRef] [PubMed]
7. Yadav, S.M. Au-Al_2O_3-Coated Highly Sensitive Broad-Range Refractive Index Sensor for Detecting Malaria Disease in Human Blood. *IEEE Sens. J.* **2024**, *24*, 23754–23763. [CrossRef]
8. Hoque, A.M.T.; Al-tabatabaie, K.F.; Ali, M.E.; Arshad, A.; Mitu, S.S.I.; Qureshi, K.K. U-grooved selectively coated and highly sensitive PCF-SPR sensor for broad range analyte RI detection. *IEEE Access* **2023**, *11*, 74486–74499. [CrossRef]
9. Wang, F.; Wei, Y.; Han, Y. High sensitivity and wide range refractive index sensor based on surface plasmon resonance photonic crystal fiber. *Sensors* **2023**, *23*, 6617. [CrossRef] [PubMed]

10. Han, B.; Zhang, Y.N.; Wang, X.; Yang, D.; Liu, Y.; Sun, J. High-sensitive fiber anemometer based on surface plas mon resonance effect in photonic crystal fiber. *IEEE Sens. J.* **2019**, *19*, 3391–3398. [CrossRef]
11. Liu, D.; Kumar, R.; Wei, F.; Han, W.; Mallik, A.K.; Jinhui, Y. Highly sensitive twist sensor based on partially silver coated hollow core fiber structure. *J. Light. Technol.* **2018**, *36*, 3672–3677. [CrossRef]
12. Han, H.; Hou, D.; Luan, N.; Bai, Z.; Song, L.; Liu, J.; Hu, Y. Surface plasmon resonance sensor based on dual-side polished microstructured optical fiber with dual-core. *Sensors* **2020**, *20*, 3911. [CrossRef] [PubMed]
13. Shuai, B.; Xia, L.; Zhang, Y.; Liu, D. A multi-core holey fiber based plasmonic sensor with large detection range and high linearity. *Opt. Exp.* **2012**, *20*, 5974–5986. [CrossRef] [PubMed]
14. Wang, W.; Zheng, Z.; Yang, C.; Fang, Z.; Wang, S.; Yuen, C. Laser-induced surface acoustic wave sensing-based malaria parasite detection and analysis. *IEEE Trans. Instrum. Meas.* **2022**, *71*, 4001609. [CrossRef]
15. Wang, S.; Wang, W.; Zheng, Y. Reconfigurable multimode microwave sensor with resonance and transmission sensing capabilities for noninvasive glucose monitoring. *IEEE Trans. Microw. Theory Tech.* **2023**, *72*, 3102–3117. [CrossRef]
16. Mittal, S.; Saharia, A.; Ismail, Y.; Petruccione, F.; Bourdine, A.V.; Morozov, O.G.; Demidov, V.V.; Yin, J.; Singh, G.; Tiwari, M. Spiral shaped photonic crystal fiber-based surface plasmon resonance biosensor for cancer cell detection. *Photonics* **2023**, *10*, 230. [CrossRef]
17. Gangwar, R.K.; Min, R.; Kumar, S.; Li, X. GeO_2 doped optical fiber plasmonic sensor for refractive index detection. *Front. Phys.* **2011**, *9*, 707113. [CrossRef]
18. Jha, R.; Sharma, A.K. High-performance sensor based on surface plasmon resonance with chalcogenide prism and aluminum for detection in infrared. *Opt. Lett.* **2009**, *34*, 749. [CrossRef] [PubMed]
19. Agarwal, S.; Giri, P.; Prajapati, Y.K.; Chakrabarti, P. Effect of surface roughness on the performance of optical SPR sensor for sucrose detection: Fabrication, characterization, and simulation study. *IEEE Sens. J.* **2016**, *16*, 8865–8873. [CrossRef]
20. Xu, H.; Song, Y.; Zhu, P.; Zhao, W.; Liu, T.; Wang, Q.; Zhao, T. Alcohol sensor based on surface plasmon resonance of ZnO nanoflowers/Au structure. *Materials* **2021**, *15*, 189. [CrossRef] [PubMed]
21. Lu, M.; Peng, W.; Liu, Q.; Liu, Y.; Li, L.; Liang, Y.; Masson, J.-K. Dual channel multilayer-coated surface plasmon resonance sensor for dual refractive index range measurements. *Opt. Exp.* **2017**, *25*, 8563–8570. [CrossRef] [PubMed]
22. Sun, M.; Song, Y.; Wu, H.; Wang, Q. Design and simulation of Au/SiO_2 nanospheres based on SPR refractive index sensor. *Sensors* **2023**, *23*, 3163. [CrossRef] [PubMed]
23. Liu, X.; Jiang, H.; Ye, J.; Zhao, C.; Gao, S.; Wu, C.; Li, C.; Li, J.; Wang, X. Nitrogen-doped carbon quantum dot stabilized magnetic iron oxide nanoprobe for fluorescence, magnetic resonance, and computed tomography triple-modal in vivo bioimaging. *Adv. Funct. Mater.* **2016**, *26*, 8694–8706. [CrossRef]
24. Timofeeva, E.; Komarova, L.; Martynenko, V.; Vasiliev, A. Indium tin oxide thin films for gas sensor applications. *Russ. Microelectron.* **2019**, *37*, 117–123.
25. Remzova, M.; Zouzelka, R.; Brzicova, T.; Vrbova, K.; Pinkas, D.; Rossner, P.; Topinka, J.; Rathousky, J. Toxicity of TiO_2, ZnO, and SiO_2 nanoparticles in human lung cells: Safe-by-design development of construction materials. *Nanomaterials* **2019**, *97*, 968. [CrossRef] [PubMed]
26. Hassanpou, P.; Panahi, Y.; Ebrahimi-Kalan, A.; Akbarzadeh, A.; Davaran, S.; Nasibova, A.N.; Khalilov, R.; Kavetsky, T. Biomedical applications of aluminium oxide nanoparticles. *Micro Nano Lett.* **2018**, *13*, 1227–1231. [CrossRef]
27. Rajendran, S.; Palani, G.; Shanmugam, V.; Trilaksanna, H.; Kannan, K.; Nykiel, M.; Korniejenko, K.; Marimuthu, U. A review of synthesis and applications of Al_2O_3 for organic dye degradation/adsorption. *Molecules* **2023**, *28*, 7922. [CrossRef] [PubMed]
28. Gudkov, S.V.; Burmistrov, D.E.; Smirnova, V.V.; Semenova, A.A.; Lisitsyn, A.B. A mini review of antibacterial properties of Al_2O_3 nanoparticles. *Nanomaterials* **2022**, *12*, 2635. [CrossRef] [PubMed]
29. Pimenta, P.F.P.; Orfano, A.; Bahia, A.C.; Duarte, A.P.M.; Rios-Velasquz, C.M.; Melo, F.F.; Pessoa, F.A.C.; Oliveira, G.A.; Campos, K.; Villegas, L.E.M.; et al. An overview of malaria transmission from the perspective of Amazon anopheles vectors. *Mem. Inst. Oswaldo Cruz* **2015**, *110*, 23–47. [CrossRef] [PubMed]
30. Suthar, B.; Bhargava, A. Biosensor application of one-dimensional photonic crystal for malaria diagnosis. *Plasmonics* **2021**, *16*, 59–63. [CrossRef]
31. Tangpukdee, N.; Duangdee, C.; Wilairatana, P.; Krudsood, S. Malaria diagnosis: A brief review. *Korean J. Parasitol.* **2009**, *47*, 93. [CrossRef] [PubMed]
32. Chaudhary, V.S.; Kumar, D.; Kumar, S. Gold-immobilized photonic crystal fiber-based SPR biosensor for detection of malaria disease in human body. *IEEE Sens. J.* **2021**, *21*, 17800–17807. [CrossRef]
33. Bendib, S.; Bendib, C. Photonic crystals for malaria detection. *J. Biosens. Bioelectron.* **2018**, *9*, 1000257. [CrossRef]
34. Weber, M.; Mulholland, E.; Jaffar, S.; Troedsson, H.; Gove, S.; Greenwood, B. Evaluation of an algorithm for the integrated man agement of childhood illness in an area with seasonal malaria in the Gambia Laboratory diagnosis of malaria. *Bull. World Health Organ.* **1997**, *75*, 25–32. [CrossRef] [PubMed]

35. Warhurst, D.C.; Williams, J.E. Laboratory diagnosis of malaria. *J. Clin. Pathol* **1996**, *49*, 533–538. [CrossRef]
36. Clendennen, T.E.; Long, G.W.; Baird, J.K. QBC® and giemsa-stained thick blood films: Diagnostic performance of laboratory technologists. *Trans. R. Soc. Trop. Med. Hyg.* **1995**, *89*, 183–184. [CrossRef] [PubMed]
37. She, R.C.; Rawlins, M.L.; Mohl, R.; Perkins, S.L.; Hill, H.R.; Litwin, C.M. Comparison of immunofluorescence antibody testing and two enzyme immunoassays in the serologic diagnosis of malaria. *J. Travel Med.* **2007**, *14*, 105–111. [CrossRef] [PubMed]
38. Poon, L.L.; Wong, B.W.; Ma, E.H.; Chan, K.H.; Chow, L.M.; Abeyewickreme, W.; Tangpukdee, N.; Yuen, K.Y.; Guan, Y.; Looareesuwan, S.; et al. Sensitive and inexpensive molecular test for falciparum malaria: Detecting plasmodium falciparum DNA directly from heat-treated blood by loop-mediated isothermal amplification. *Clin. Chem.* **2006**, *52*, 303–306. [CrossRef] [PubMed]
39. Rahman, M.M.; Molla, M.A.; Paul, A.K.; Based, M.A.; Rana, M.A.; Anower, M.S. Numerical investigation of a highly sensitive plasmonic refractive index sensor utilizing hexagonal lattice of photonic crystal fiber. *Results Phys.* **2020**, *18*, 103313. [CrossRef]
40. Chaudhary, V.S.; Kumar, D.; Mishra, R.; Sharma, S. Twin core photonic crystal fiber for temperature sensing. *Mater. Today Proc.* **2020**, *33*, 2289–2292. [CrossRef]
41. Haripriya, N.; Mondal, H.; Haldar, B.; Swarnakar, S. Advancements and challenges in photonic crystal fibre-based sensors for biomedical applications. *Sens. Bio-Sens. Res.* **2026**, *52*, 100953. [CrossRef]
42. Chaudhary, V.S.; Kumar, D. TOPAS based porous core photonic crystal fiber for terahertz chemical sensor. *Optik* **2020**, *223*, 165562. [CrossRef]
43. Mishra, G.P.; Kumar, D.; Chaudhary, V.S.; Sharma, S. Terahertz refractive index sensor with high sensitivity based on two-core photonic crystal fiber. *Microw. Opt. Technol. Lett.* **2021**, *63*, 24–31. [CrossRef]
44. Liu, P.Y.; Chin, L.K.; Ser, W.; Chen, H.F.; Hsieh, C.-M.; Lee, C.-H.; Sung, K.-B.; Ayi, T.C.; Yap, P.H.; Liedberg, B.; et al. Cell refractive index for cell biology and disease diagnosis: Past, present and future. *Lab Chip* **2016**, *16*, 634–644. [CrossRef] [PubMed]
45. Yesudasu, V.; Pradhan, H.S.; Pandya, R.J. Recent progress in surface plasmon resonance based sensors: A review. *Heliyon* **2021**, *7*, e06321. [CrossRef] [PubMed]
46. Rafi, H.N.; Kaysir, M.R.; Islam, M.J. Air-hole attributed performance of photonic crystal fiber based SPR sensors. *Sens. Bio Sens. Res.* **2020**, *29*, 100364. [CrossRef]
47. Park, Y.; Diez-Silva, M.; Popescu, G.; Lykotrafitis, G.; Choi, W.; Feld, M.S.; Suresh, S. Refractive index maps and membrane dynamics of human red blood cells parasitized by plasmodium falciparum. *Proc. Nat. Acad. Sci. USA* **2008**, *105*, 13730–13735. [CrossRef] [PubMed]
48. Kumar, B.M.H.; Srikanth, P.C.; Vaibhav, A.M. A novel computation method for detection of malaria in RBC using photonic biosensor. *Int. J. Inf. Technol.* **2021**, *13*, 2053–2058. [CrossRef] [PubMed]
49. Rashidnia, A.; Pakarzadeh, H.; Hatami, M.; Ayyanar, N. Photonic crystal-based biosensor for detection of human red blood cells parasitized by plasmodium falciparum. *Opt. Quantum Electron.* **2022**, *54*, 38. [CrossRef]
50. Mohammed, N.A.; Hamed, M.M.; Khalaf, A.A.M.; El-Rabaie, S. Malaria biosensors with ultra-sensitivity and quality factor based on cavity photonic crystal designs. *Eur. Phys. J. Plus* **2020**, *135*, 933. [CrossRef]
51. Sen, S.; Shafi, M.A.A.; Mubassera, M.; Hawlader, M.T.H. A High-Sensitivity Photonic Crystal Fibre Biosensor for Malaria Detection. *Sens. Bio Sens. Res.* **2026**, *51*, 100963. [CrossRef]
52. Abdullah-Al-Shafi, M.; Sen, S.; Mubassera, M. Machine learning assisted malaria detection using photonic crystal fibre optical sensors. *Sci. Rep.* **2026**, *16*, 8320. [CrossRef] [PubMed]
53. Shafkat, A.; Rashed, A.N.Z.; Hageen, H.M.; Alatwi, A.M. Design and analysis of a single elliptical channel photonic crystal fiber sensor for potential malaria detection. *J. Sol.-Gel. Sci. Technol.* **2021**, *98*, 202–211. [CrossRef]
54. Chaudhary, V.; Singh, S. Design and optimization of a terahertz photonic crystal fiber based biosensor to detect malaria disease. *J. Comput. Electron.* **2025**, *24*, 1. [CrossRef]
55. Srivastava, R.; Prajapati, Y.K.; Pal, S.; Kumar, S. Micro-channel plasmon sensor based on a D-shaped photonic crystal fiber for malaria diagnosis with improved performance. *IEEE Sens. J.* **2022**, *22*, 14834–14841. [CrossRef]
56. Sharma, A.K.; Jha, R.; Gupta, B.D. Fiber-optic sensors based on surface plasmon resonance: A comprehensive review. *IEEE Sens. J.* **2007**, *7*, 1118–1129. [CrossRef]
57. Lou, J.; Cheng, T.; Li, S.; Zhang, X. Surface plasmon resonance photonic crystal fiber biosensor based on gold-graphene layers. *Opt. Fiber Technol.* **2019**, *50*, 206–211. [CrossRef]
58. Zhang, Y.-X.; Lin, Q.; Yan, X.; Wang, L.; Liu, G.-D. Flat-band Friedrich-Wintgen bound states in the continuum based on borophene metamaterials. *Opt. Exp.* **2024**, *32*, 10669–10678. [CrossRef] [PubMed]
59. Hassen, M.N.; Ferdous, M.; Khalek, M.A.; Chakma, S.; Paul, B.K.; Ahmed, K. Design and analysis of biosensor based on surface plasmon resonance. *Sens. Biosens. Res.* **2018**, *21*, 1–6. [CrossRef]
60. Hajiani, T.; Shirkani, H.; Sadeghi, Z. Surface plasmon resonance photonic crystal fiber biosensor: Utilizing silver-phosphorene nanoribbons for near-IR detection. *Opt. Commun.* **2024**, *569*, 130801. [CrossRef]

61. Haripriya, N.; Murali, Y.T.; Dubey, S.K.; Swarnakar, S.; Kumar, S. AI-integrated photonic crystal fiber-based devices. In *Intelligent Photonics Systems*; CRC Press: Boca Raton, FL, USA, 2025; pp. 14–51. [CrossRef]
62. Chao, C.T.C.; Chau, Y.-F.C. Engineering plasmonic photonic crystal fiber sensor: Design, fabrication strategies and performance roadmap. *Mater. Sci. Eng. B* **2026**, *324*, 119046. [CrossRef]

Disclaimer/Publisher's Note: The statements, opinions and data contained in all publications are solely those of the individual author(s) and contributor(s) and not of MDPI and/or the editor(s). MDPI and/or the editor(s) disclaim responsibility for any injury to people or property resulting from any ideas, methods, instructions or products referred to in the content.